Hydro-geomorphic metrics for high resolution fluvial landscape analysis

Thomas Bernard, Philippe Davy, Dimitri Lague

JGR Earth Surface

RESEARCH ARTICLE
10.1029/2021JF006535

Hydro-Geomorphic Metrics for High Resolution Fluvial Landscape Analysis

Thomas G. Bernard[1], **Philippe Davy**[1], **and Dimitri Lague**[1]

[1]CNRS, Géosciences Rennes – UMR 6118, Université de Rennes, Rennes, France

Key Points:

- We use a 2D hydraulic model on a 1 m Digital Elevation Model and derive hydro-geomorphic metrics of slope, drainage area and river width
- Analyses of scaling laws based on these metrics provide a better identification of hillslopes and channels than a traditional approach
- A multi-runoff approach allows to characterize the hydraulic geometry along the river network and to identify floodplains

Supporting Information:

Supporting Information may be found in the online version of this article.

Correspondence to:

T. G. Bernard,
thomas.bernard@univ-rennes1.fr

Citation:

Bernard, T. G., Davy, P., & Lague, D. (2022). Hydro-geomorphic metrics for high resolution fluvial landscape analysis. *Journal of Geophysical Research: Earth Surface*, *127*, e2021JF006535. https://doi.org/10.1029/2021JF006535

Received 24 NOV 2021
Accepted 7 MAR 2022

Author Contributions:

Conceptualization: Thomas G. Bernard, Philippe Davy, Dimitri Lague
Formal analysis: Thomas G. Bernard
Funding acquisition: Philippe Davy, Dimitri Lague
Investigation: Thomas G. Bernard
Methodology: Thomas G. Bernard, Philippe Davy, Dimitri Lague
Project Administration: Philippe Davy, Dimitri Lague
Software: Philippe Davy
Supervision: Philippe Davy, Dimitri Lague
Validation: Philippe Davy, Dimitri Lague
Visualization: Thomas G. Bernard
Writing – original draft: Thomas G. Bernard
Writing – review & editing: Philippe Davy, Dimitri Lague

Abstract Topographic metrics are designed to quantify scale-relevant relationships between geometric properties of landscapes to reveal the processes shaping them. They have long been derived from topographic flow routing algorithms, initially developed for coarse Digital Elevation Models (DEMs), whose resolution (≥30 m) and poor precision did not resolve correctly flow patterns and channel flow width. Since high resolution and precision DEMs make the description of meter-scale flow patterns possible, new methods are required to analyze high resolution landforms structures such as hillslope-channel connections, channel width or floodplains. Here, we investigate the potential of 2D hydraulic simulations based on the shallow water equations to replace the classical slope versus drainage area analysis, to analyze river morphology and to identify floodplains. We apply the Floodos model to the 1 m resolution DEM of the Elder Creek catchment, California, from which we derive three hydro-geomorphic metrics accounting for the river geometry: a specific drainage area extended to channels, an effective flow width and the hydraulic slope. We analyze the Elder Creek catchment through what we call the hydraulic slope-area diagram allowing a better identification of hillslope-channel connections than the slope-area approach. The effective flow width is analyzed along the drainage network and is characterized by a power-law relationship consistent with previous observations. We derive metrics based on a multi-runoff approach to automatically identify floodplains and evaluate along-stream variations in hydraulic geometry. The hydro-geomorphic metrics offer a geomorphic analysis suitable for high resolution DEMs and opens up new perspectives in fluvial landscape analysis.

Plain Language Summary Landform analysis is essential to identify and understand the processes shaping landscapes. It is traditionally based on topographic metrics following surface flow paths designed to reveal surface processes and to characterize the spatial organization of landscapes through scale-relevant relationships. Current methods to compute these metrics are not able to resolve both high resolution flow patterns and width. New methods are required to analyze fine scale landforms structures such as hillslope-channel connections, channel width or floodplains. We investigate the potential of 2D hydraulic simulations, which consists in simulating water depth and velocity on the topographic surface, to analyze such landform structures. We applied the Floodos model to a meter-scale resolution topographic data from the Elder Creek catchment in California. We demonstrate that 2D hydraulic simulation allows to better identify hillslope-channel connections than traditional approach and to easily estimate river flow width through the use of derived hydro-geomorphic metrics. The analysis of these metrics at various input discharges enables to support description of floodplains and along-stream variations in hydraulic geometry allowing a richer description of landscape organization. The use of 2D hydraulic simulation opens up new perspectives to analyze high resolution landform structures crucial in the understanding of processes controlling landscape evolution.

1. Introduction

Fluvial landscape analysis is based on computing topographic metrics designed to quantify geometric properties of landforms. These metrics have been used to derive scale-relevant relationships to reveal the links between surface processes, tectonic and climatic forcings and the resulting landforms, as well as to identify spatial organization of the landscape. Among others, slope (S) and drainage area (A) have long been used as topographic metrics to identify the dominant erosion processes in a catchment (e.g., Hack, 1957; Ijjasz-Vasquez & Bras, 1995; Montgomery & Foufoula-Georgiou, 1993; Royden et al., 2000; Tarolli & Dalla Fontana, 2009; Willgoose et al., 1991). For instance, Montgomery and Foufoula-Georgiou (1993) proposed a partionning of the landscape into three geomorphic domains based on inflections of the mean slope-area (S-A) relationship in a log-log diagram: convex hillslopes, unchanneled valleys and fluvial domain. Subsequent work has focused on using the S-A diagram to identify channel heads (McNamara et al., 2006; Orlandini et al., 2011; Tarolli & Dalla Fontana, 2009), landslides

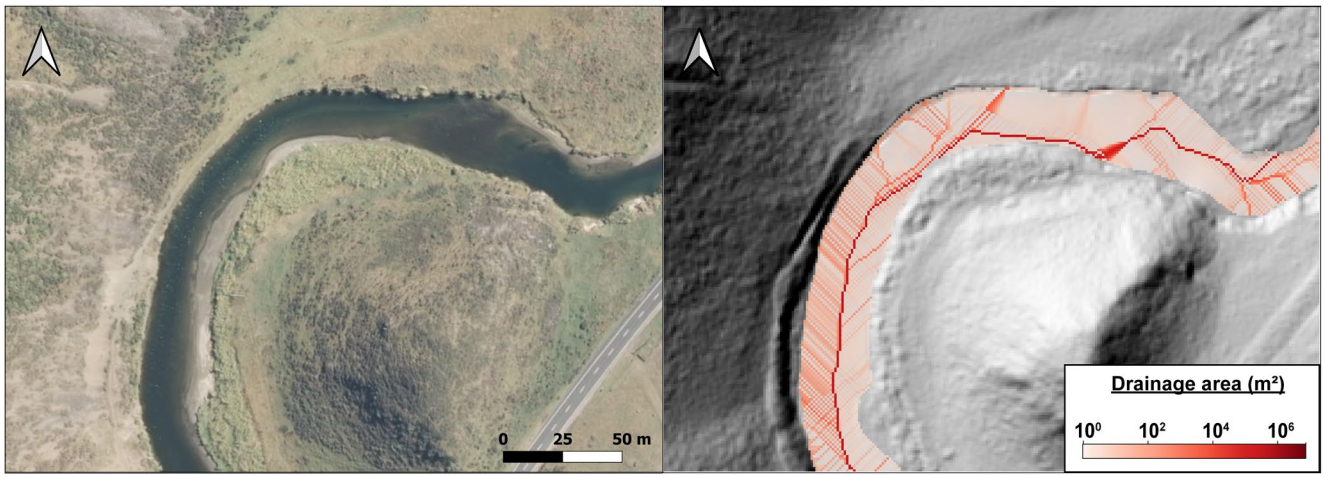

Figure 1. Aerial photo of a river near Wellington in New Zealand (left; LINZ, 2014) and the 1 m resolution LiDAR DEM (right; LINZ, 2017) showing drainage area values calculated by a D∞ flow routing where the river is wider than the grid resolution. Location: 1757118; 5414793 (NZTM2000).

and debris flows processes (Booth et al., 2013; Lague & Davy, 2003; Stock & Dietrich, 2003, 2006) or the presence of vegetation (Istanbulluoglu & Bras, 2005). In all of these approaches, the fluvial domain occurs beyond a critical drainage area, typically ranging from 0.1 to 1 km^2 (Ijjasz-Vasquez & Bras, 1995; Tarolli & Dalla Fontana, 2009), and is generally characterized by a power-law decrease of topographic slope with drainage area (Flint, 1974):

$$S = k_s.A^{-\theta} \quad (1)$$

where k_s is the steepness index and θ the concavity index. The steepness index is a classical metric of erosion intensity in tectonic geomorphology (e.g., Kirby & Whipple, 2012; Lague, 2014; Snyder et al., 2000, 2003), illustrating the fundamental link between landscape form and erosion processes.

These topographic metrics are derived from flow routing algorithms based on the topographic slope (i.e., D8 or D∞) initially developed for coarse digital elevation models (DEMs), whose resolution is typically between 10 and 100 m. Along the channel network, the D8 and D∞ algorithms provide a graph of the flow paths, which is a reasonable estimate of the actual surface flows in the case of channel widths smaller than the DEM resolution. The introduction of high resolution DEMs (HRDEM) from airborne Light-Detection and Ranging (LiDAR) techniques has considerably increased the vertical accuracy (<20 cm) and the channel resolving capacity (pixel size <2 m) that coarse DEM cannot offer (Passalacqua et al., 2015; Roering et al., 2013; Tarolli, 2014). This increased resolution and precision make the description of the internal structure of flow in channels possible, opening new venues to better identify subtle topographic signals and geomorphic domains (Tarolli & Dalla Fontana, 2009). Yet, with this DEM resolution, traditional flow routing algorithms fail to capture the morphology of rivers wider than the resolution: they concentrate the total river discharge (or drainage area) in one or few pixels along the channel section while others have unrealistic low discharges even with a D∞ flow algorithm (Tarboton, 1997; Figure 1). Therefore, the channel network derived from the *S-A* analysis is a 1D skeleton river network independent of channel width, with incorrect flow paths connecting hillslopes, valleys, channels, and floodplains. Channel width in particular cannot be readily extracted from traditional flow routing algorithms while it is a geometrical characteristic of rivers as important as channel slope (e.g., Croissant et al., 2017; Finnegan et al., 2007). Several methods to extract channel width exist based on high resolution aerial or satellite images (Fisher et al., 2013; Güneralp et al., 2014; Pavelsky & Smith, 2008; Rowland et al., 2016; Schwenk et al., 2017, 2020). These methods can only measure the channel width as the free water surface extent at the time of image acquisition, which may not be geomorphologically relevant, and the measurement remains unfeasible in areas with dense vegetation cover. HRDEM-based methodologies can estimate channel width by detecting the extent of channel banks based on topographic slope (Johansen et al., 2011; Passalacqua et al., 2012; Zheng et al., 2019) or curvature (Sofia et al., 2015), but they generally need some parameter tuning and can only measure the bankfull width independently of any reference flow. While these HRDEM-based methods showed good

agreement with measurements for single thread and meandering channels with well-defined banks, their efficiency when applied on more complex channel geometries such as braided rivers or rivers with multiple channels is uncertain. Hence, new tools and methods are required to address the significant change in DEM resolution and the calculation of channel width.

The increase in computational power and model efficiency now permits to directly model the surface water flow on HRDEM by solving mass and momentum equations. Due to its capability to represent physical overland flow, the two-dimensional depth integrated shallow water equations (SWEs) model is recognized as the most suitable approach to perform runoff computation on HRDEM (Bellos & Tsakiris, 2016; Bout & Jetten, 2018; Cea et al., 2010, 2014; Costabile et al., 2012). The increase in model efficiency and the increasing availability of LiDAR data facilitate the application of such models to HRDEM at a catchment scale (Coulthard et al., 2013; David & Schmalz, 2020; Davy et al., 2017; Neal et al., 2018). This application provides new opportunities to analyze landscapes beyond the 1D skeleton channel structure offered by traditional flow routing algorithms, which can now be replaced by a 2D description of the flow geometry that is closer to reality. For instance, Costabile et al. (2019) and Costabile and Costanzo (2021) recently used the 2D SWEs model to analyze scaling laws by comparing the water depth or the specific discharge threshold to a dimensionless area to identify the extent of the river network. The authors highlighted the added value of using 2D hydraulic simulation at the catchment scale for the identification of channel heads and the determination of the hydrodynamic behavior of the river network with many implications for the understanding of environmental processes.

The aim of this study is to investigate the potential of 2D hydraulic simulation to (a) identify hillslopes, valleys and river channels in a manner similar to the traditional *S-A* analysis, (b) characterize river morphology, including channel width and hydraulic geometry, and (c) identify floodplains and knickpoints. We replace classical topographic metrics by hydro-geomorphic metrics using the modeled hydraulic water surface enabled by the fine resolution LiDAR data. To this end, we apply the hydrodynamic component of the 2D morpho-hydrodynamic model Riverlab (formerly Eros; Crave & Davy, 2001; Davy & Lague, 2009) called Floodos (Davy et al., 2017) on the Elder Creek catchment located in California, USA. This catchment exhibits sufficiently wide river channels (up to 15 m) with alongside pronounced floodplains, has been surveyed by a topographic airborne LiDAR providing a 1 m resolution DEM, and is monitored by a USGS gauging station. Compared to a widely use model such as 2D LISFLOOD-FP (Bates et al., 2010; Coulthard et al., 2013), Floodos showed better time efficiency (Davy et al., 2017; Hocini et al., 2021). It can be directly applied on a DEM without pre-processing.

The paper is organized as follow. We first present the Floodos model, the Elder Creek catchment and the initial conditions of the hydraulic simulations. Next, we introduce three hydro-geomorphic metrics. The first one corresponds to a normalized discharge per unit width that is related to the widely used concept of the specific drainage area a_s previously defined on hillslopes (Beven & Kirkby, 1979; Gallant & Hutchinson, 2011; Quinn et al., 1991, 1995), that is now extended to channels. We also define an effective flow width $w(r)$ and the hydraulic slope S_h. These hydro-geomorphic metrics are respectively compared with the classical drainage area, the water surface width defined by the model and the classical topographic slope. In another section, the Elder Creek catchment is first analyzed through what we call the hydraulic slope-area diagram and compared with the classical *S-A* diagram in terms of identification of geomorphic domains. We also analyze the river network through the relationship between the effective flow width and the drainage area. The sensitivity of these approaches to the DEM resolution is analyzed and a multi-runoff analysis is performed to identify discharge-dependent geomorphic domains, in particular floodplains. Finally, we discuss and conclude on the added value brought by each hydro-geomorphic metrics and their relationships to high resolution fluvial landscape analysis.

2. Methods

2.1. The Precipiton Model: A Particle-Based Approach for Solving 2D SWEs

Riverlab (formerly Eros) is a 2D morpho-hydrodynamic model based on a particle approach called precipiton (Davy et al., 2017). In this paper, only the hydrodynamic component of Riverlab called Floodos is used. We hereafter present a succinct description of the model but further details can be found in Davy et al. (2017). Precipitons are elementary water volume particles that mimic the path of water droplets on top of the topography and water surface. The model solves the SWEs in the precipiton framework to calculate both river depth and discharge. It has been developed for the diffusive wave approximation, that is, without inertial terms, and can be

directly applied on a DEM. The downstream direction of the precipitons is stochastically set with a probability proportional to the directional discharge, that is, the discharge calculated with the surface water slope in the considered direction. The water volume in each cell is increased at each precipiton passage by the precipiton volume and decreased between two passages according to the friction equation. The interplay between the water surface dynamics and the precipiton paths leads to a fairly efficient solution of the equilibrium stress equation where friction equilibrates with gravity. Proofs of the convergence of the method to the hydraulic solution are given in Davy et al. (2017). The method can be used in two ways. In unsteady mode, the volume of water in each precipiton evolves step by step to reach the water balance in each cell; in stationary mode, the precipiton keeps its initial volume all along the path and the mass balance is obtained when the surface tends to an equilibrium state. The second mode is the fastest; it allows for example, a single precipiton to fill a lake in a hole of the topography whatever its size. The calculations performed in this study were done in stationary mode.

The key relationship for the SWEs in the diffusive wave approximation is the shear friction on topography, which is expressed as:

$$\boldsymbol{\tau} = K(h)|u|\boldsymbol{u} \tag{2}$$

where $\boldsymbol{\tau}$ and $\boldsymbol{u}$ are the components of the shear stress and water velocity vectors, respectively, and h is the water depth. $K(h)$ is a dimensionless friction function that is found to be slightly dependent on h in experiments (Manning, 1891) or modeled as a constant coefficient (Darcy-Weisbach). K is also dependent on the roughness of the river bed. The velocity and water depth vary so that the shear stress exactly balances the gravity force $\rho g h s_h$, where ρg is the unit weight of water and $\boldsymbol{s_h}$ the hydraulic slope vector. This leads to the friction equation that gives the water velocity as a function of the hydraulic slope which, in the case of Manning's equation is written:

$$\boldsymbol{u} = \frac{h^{2/3}\,\boldsymbol{s_h}}{n\sqrt{|s|}} \tag{3}$$

where n is the friction coefficient that varies between 0.025 and 0.05 for sediment beds (Arcement & Schneider, 1989) and s is the steepest topographic slope.

The calculation requires to specify as inputs a map of friction coefficients and runoffs. The output variables are the maps of water level h and specific discharges $q = uh$. An important aspect of the precipiton method is the choice of the input precipiton volume $\overline{V^p}$ which sets the amplitude of the hydraulic surface fluctuations. If $\overline{V^p}$ is too large, the fluctuations can lead to bias in the hydraulic slope distribution that will affect both the calculation of discharges and the routing of precipitons, leading to incorrect numerical solutions. Conversely, the calculation time is inversely proportional to $\overline{V^p}$, which implies that the user needs to select $\overline{V^p}$ large enough to have reasonable computation times but not too large so that the solution remains correct. Davy et al. (2017) proposed a stability criterion to avoid the bias due to large fluctuations of the water surface defined as follow:

$$\frac{\overline{V^p}}{\Delta x \Delta y} \ll S_h \Delta x \tag{4}$$

This criterion requires to define a hydraulic slope S_h a priori, and will be discussed in Section 2.3.

The elements presented in this section provide the basic components of the model and constitute the essence of our approach. Floodos has already demonstrated its ability to deal with HRDEMs resolving channel complexity, pits and dams (Davy et al., 2017; Hocini et al., 2021), supporting its potential to meet the purpose of this paper.

2.2. Study Area

To illustrate the potential of 2D hydraulic simulation in landscape analysis using HRDEM, we calculate the flow characteristics on the 16.7 km^2 Elder Creek watershed located in northern California, USA. This watershed has several attributes that make it perfect for our analysis: (a) a topographic LiDAR DEM at 1 m resolution is freely available (Dietrich, 2014, last access: 22 November 2021) (b) it presents sufficiently wide channels (up to 15 m), (c) it is monitored by an USGS gauging station, and (d) it has been studied in previous field investigations (Fuller et al., 2009; Lovill et al., 2018; Scheingross et al., 2013; Seidl & Dietrich, 1992). This watershed is located in the Angelo Coast Range Reserve, and it experiences a Mediterranean climate. PRISM data from 1981 to 2010

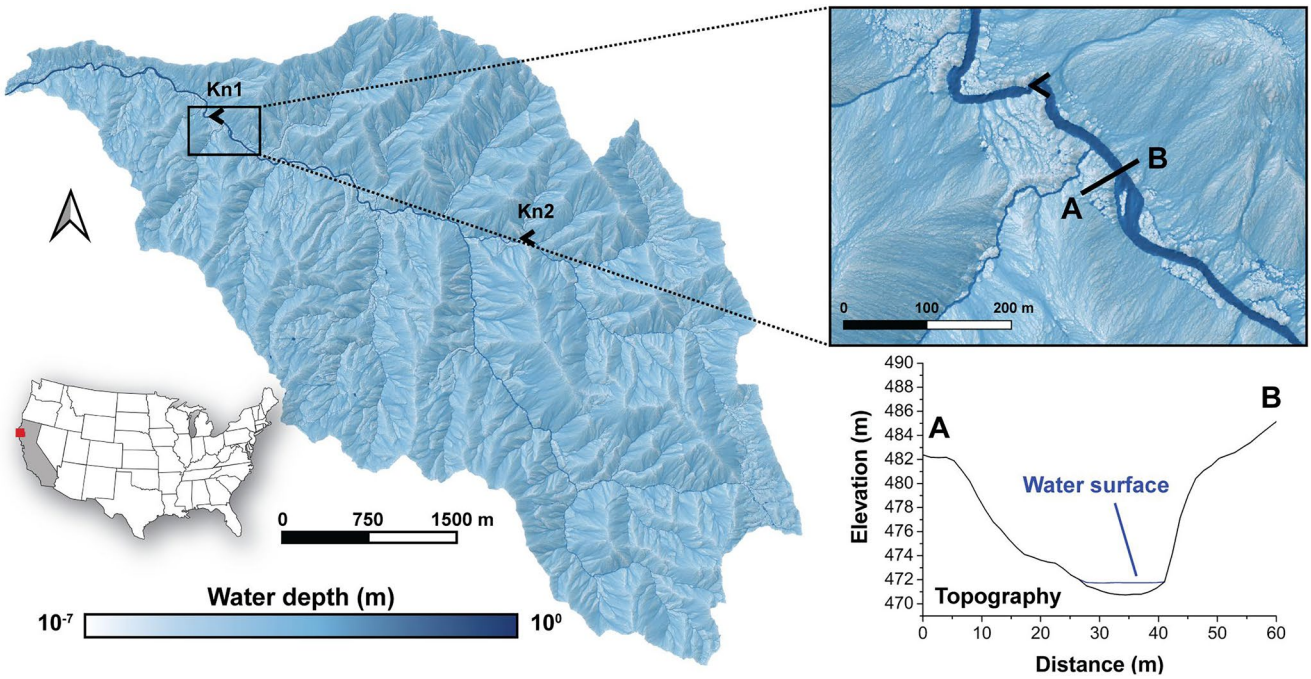

Figure 2. Simulated water depth resulting from the Riverlab model applied to the Elder Creek catchment located in California, USA. The water depth is superimposed on the LiDAR-DEM of the Elder Creek basin. Kn1 and Kn2 are two knickpoints. A cross-section of the river with the water surface is shown.

indicate a mean annual precipitation and temperature of 2,042 mm and 12.4°C respectively (PRISM, 2010). The daily mean runoff rate, deduced from USGS gauge station discharge data from 1967 to 2019, spans from 10^{-3} to 10 mm/hr (Figure S1 in Supporting Information S1).

Elder Creek is characterized by a bedrock dominated channel network along where channel incision (0.2–0.4 mm/yr; Fuller et al., 2009) during the Late Paleocene-Holocene period led to the formation of pronounced strath terraces and steep hillslopes (Lovill et al., 2018; Seidl & Dietrich, 1992). The channel bed is composed of short patches of bare bedrock and long reaches of coarse gravel-, cobble-, and boulder-sized alluvium along the first 4 km upstream from the outlet. Upstream, boulders of several meters in diameter, small boulders and cobbles associated with cascades and pools become very common due to the occurrence of landslides and debris flows as described by Seidl and Dietrich (1992). These authors also noticed a pronounced knickpoint 7 m high located at 2.3 km (Kn1) from the outlet (Figure 2). We noticed another knickpoint about 20 m high (Kn2) in the upper 4 km.

2.3. Modeling Approach and Assumptions

The modeling approach considered here aims at routing surface flow on HRDEM while accounting for the filling of holes, and the spreading of water in rivers. By resolving a water surface, we view the hydraulic simulation as a more appropriate approach to solve for a flow routing on HRDEM than traditional methods. As such, we do not aim at a strict hydrological modeling and only aim at using the topography without accessory data such as soil depth, groundwater table, vegetation cover, variable friction maps etc. Consequently, the modeling is intentionally simplified and is based on a constant and uniform runoff rate assuming that runoff generation only results from the exceedance of infiltration capacity. Other runoff generation processes induced by groundwater flow or losses by evaporation or infiltration are not considered. Our base simulation considers a heavy runoff rate of $r = 10$ mm/hr corresponding to high flow conditions for the Elder Creek catchment (Figure S1 in Supporting Information S1). We also explore the sensitivity of the hydro-geomorphic metrics to the runoff rate exploring a range from 1 to 100 mm/hr. The Manning's friction coefficient is assumed to be uniform over the catchment area, equal to $n = 0.03$. The model is applied in a stationary mode for which the precipiton volume remains constant along its path, as defined in Davy et al. (2017). We choose a precipiton volume of 10^{-3} m^3 (or a precipiton height of 1 mm at 1 m of resolution) as (a) it respects the stability criterion (Equation 4) and (b) it allows the definition of hydraulic slope resolution down to 10^{-3} m/m, consistent with the range of topographic slopes computed on

the DEM. The resulting water depth is at steady-state condition. An example of a simulation result is given in Figure 2 showing the main difference between 1D flow routings and 2D modeling, accounting for hydrodynamics, where the channel network is no longer a single line.

3. Results

3.1. Definition of 2D Hydro-Geomorphic Metrics

3.1.1. A Specific Drainage Area Calculated for Hillslopes and Channels

In this section, we present a hydro-geomorphic metric to analyze the flow pattern for any given runoff rate r. This hydro-geomorphic metric is based on the widely used concept of the specific drainage area a_s corresponding to a discharge per unit flow width (i.e., the specific discharge). The specific drainage area has been used in combination with the topographic slope as a wetness index to describe patterns of saturation (Beven & Kirkby, 1979; Quinn et al., 1991, 1995), and as a stream power index to describe patterns of hillslope erosion (Moore & Burch, 1986; Moore & Wilson, 1992) or channel initiation (McNamara et al., 2006; Montgomery & Dietrich, 1992). It is generally calculated from the ratio between the drainage area A, derived from a D8/D∞ algorithm on topographic slope, and the flow width w estimated from contour lines:

$$a_s = \frac{A}{w} \tag{5}$$

This method has many drawbacks due to the use of flow routing algorithms based on the topographic slope, as explained before in the introduction of this paper, which limit its application to hillslopes (Gallant & Hutchinson, 2011). The use of 2D SWEs modeling allows to extend the calculation of the specific drainage area to channels and is thus defined for the entire catchment. Here, the specific drainage area is noted $a_s(r)$ as it depends on the input runoff rate r and is defined for each pixel as the ratio between the specific discharge $q(r)$ computed by Floodos and the runoff rate r (m/s) sets for the model simulation:

$$a_s(r) = \frac{q(r)}{r} \tag{6}$$

$a_s(r)$ has unit of length [m^2/m]. Recall that when the flow is channelized over a width w:

$$q(r) = \frac{Q(r)}{w(r)} = \frac{r\,A}{w(r)} \tag{7}$$

where $Q(r)$ is the total discharge computed for the chosen runoff rate r.

In channels wider than one pixel, $a_s(r)$ will be smaller than A, and the difference will increase with channel width. When the flow width is smaller than the pixel size, or when the flow is not channelized as in overland flow, Equation 5 can still be defined. In such case, $w(r)$ indicates variations between flow accumulation computed between a purely topographic algorithm and the hydraulic model computation. If the two flow patterns are similar, $w(r)$ should be of the order of 1.

To highlight the differences between a classical 1D flow routing algorithm and the 2D hydraulic modeling with the Floodos model, we compare the drainage area calculated from a D∞ flow routing (Tarboton, 1997) with $a_s(r)$ (Figure 3a). In essence, we want to highlight the differences between the calculation of a proxy for a normalized total flow discharge (A) and a proxy for the normalized discharge per unit flow width (a_s) in relation to the associated flow patterns. Drainage area and topographic slope are calculated using the TauDEM software (Tarboton, 2014). At first order, $a_s(r)$ is proportional to A ($a_s \sim A^{0.85}$ with a correlation coefficient = 0.63) highlighting that for the majority of the landscape, flow patterns computed by the D∞ algorithm and the 2D hydraulic model are broadly similar. Note that the relation between a_s and A depends on the DEM resolution; this point will be discussed in Sections 3.2.2. and 3.3.2. To account for this effect, we plotted the A/dx line in Figure 3a where dx represents the pixel size. Two important deviations occur from the A/dx line and the broad scaling relationship between a_s and A: first, for A roughly larger than 10^5 m^2, $a_s(r)$ becomes systematically smaller than A; second, for $A < 10^3$ m^2, a large fraction of the DEM pixels have specific drainage areas several orders of magnitude larger than A. These deviations stem from the fundamental differences in computing A and $a_s(r)$ in channels larger than one pixel. As shown in Figure 3b, large specific drainage areas are computed on the entire width of the channel

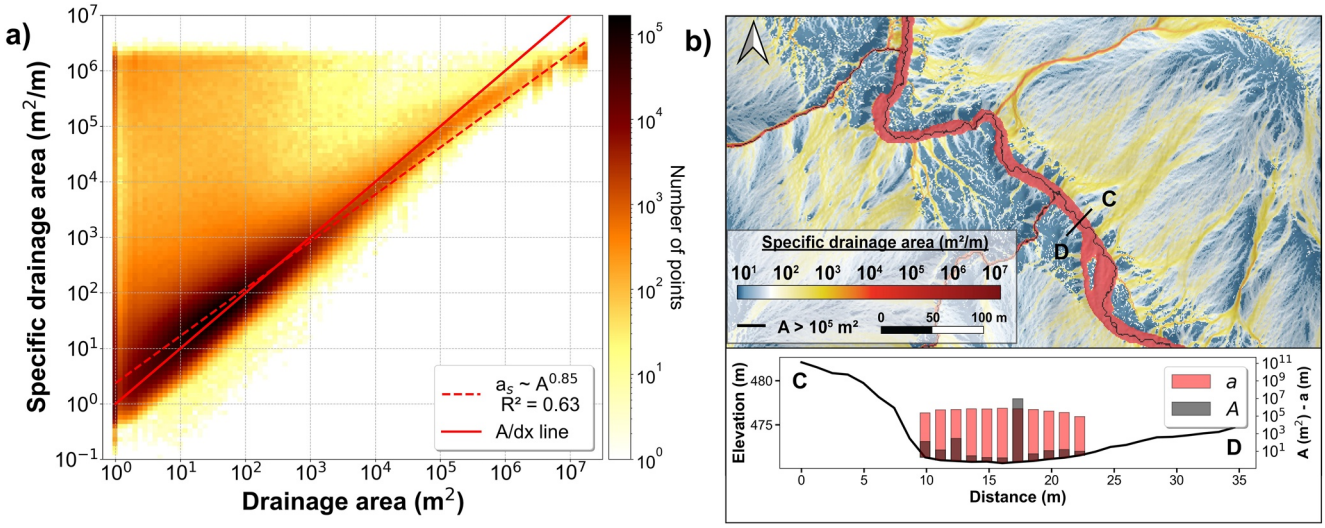

Figure 3. (a) 2D histogram between the drainage area A calculated from a D∞ flow algorithm and the specific drainage area a_s calculated from the Riverlab model for a runoff rate of 10 mm/hr. In this case, dx is equal to 1m. The A/dx line represents the ratio between the drainage area and the pixel size dx. (b) Map of a_s and cross-section perpendicular to the river showing the two variables. Values in red corresponds to $a_s > 10^5$ m²/m. Note the logarithmic scale for $a_s(r)$ and A.

while high drainage area values are systematically concentrated on a single pixel along the channel profile, even when a D∞ algorithm is used. Consequently, and as expected from Equation 5, $a_s(r) < A$ along the D∞ channel profile, while $a_s(r) >> A$ on nearby channel pixels for which an extremely low drainage area is computed (Figure 3b). In essence, the 2D hydraulic model spreads out the local peak of drainage area over the entire flooded section of the channel, accurately resolving the true extent of the channel flow computed for the input runoff rate.

3.1.2. The Effective Flow Width

As shown by Equation 5, it is possible to calculate a proxy for the flow width from the specific drainage area a_s, computed by Floodos, and the drainage area A over the entire catchment area as follow:

$$w(r) = \frac{A}{a_s(r)} \tag{8}$$

Here, the drainage area is computed with a D8 flow routing algorithm (O'Callaghan & Mark, 1984) to ensure that the total area is concentrated in a single pixel along the flow path. In this particular case, the algorithm is not applied on the topography, but rather on the specific discharge map computed by Floodos at low flow conditions (r = 1 mm/hr) to (a) have a measure of $w(r)$ for which the local maximum of A is coincident with the local maximum of a_s and (b) to measure $w(r)$ at the same location for any input runoff rate. This approach provides a simple and straightforward way to estimate $w(r)$ without the need to look for local neighbors. As described in the previous section, $w(r)$ can be calculated even though the flow is not channelized and is indicative of the variations between a topographic algorithm and the hydraulic model computations. However, in what follows we aim to illustrate the meaning of $w(r)$ only when the flow is channelized. To this end, we compare $w(r)$ to the wetted width of 35 channel cross-sections covering a range of drainage area from 8×10^4 m² to 2×10^7 m² and for which $w(r) \geq 3$ m to limit the uncertainties related to pixel size (Figure 4). The wetted width represents the simulated water surface extent measured manually along the cross-sections where the simulated water depth is at least 10 cm. For the ideal case of a purely rectangular channel with vertical banks, the flow width should equal the wetted width. Results show that $w(r)$ is close to the wetted width for channels with steep banks and narrower than about 5 m (Figures 4a and 4b1). However, $w(r)$ is systematically lower than the wetted width for larger channels. This occurs for two reasons. First, because $w(r)$ is measured from the maximum of a_s (Equation 8), and second, because of the deviation from a simple rectangular geometry generating non-uniform distributions of a_s, with wide river channels having non-vertical banks and a concave up cross-section geometry (Figure 4b2). Large deviations between $w(r)$ and the wetted width also occur for complex river bathymetry (e.g., multiple channels) and in flooded areas (Figure 4b3). These results show that $w(r)$ corresponds to the channel section over which

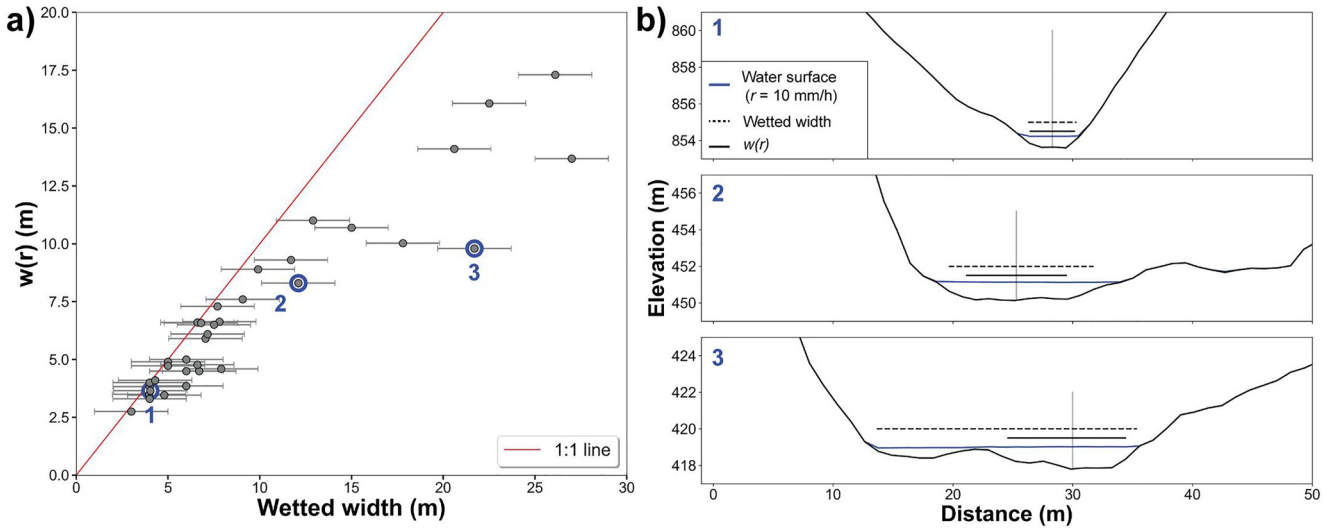

Figure 4. Effective flow width $w(r)$ versus wetted width measured for 35 cross sections along the channel network for r = 10 mm/h. (a) $w(r)$ versus wetted width. Wetted width is measured where water depth is higher than 10 cm. The measurement uncertainty of the wetted width is set to 2 m (1 pixel for each side of the channel). (b) Three cross-sections showing different channel morphologies for which: (1) $w(r)$ equals the wetted width, (2) $w(r)$ is lower than the wetted width and (3) $w(r)$ << wetted width. The number associated to each section is shown in blue in (a).

most of the flow occurs for a given runoff intensity r and thus represent an effective flow width, rather than the extent of the water surface.

3.1.3. The Hydraulic Slope

The hydraulic slope S_h is calculated from the water surface along the flow direction. It can be calculated for all pixels and compared to the topographic slope S derived from a D∞ calculation. Both the topographic and hydraulic slopes are here calculated following a pixel-by-pixel approach. A comparison between the two variables on the Elder Creek watershed shows that a large fraction of pixels (81%) fall along the 1:1 line (Figure 5a). This indicates that both variables are equal for most of the catchment area, especially on steep slopes (Figures 5a and 5b). However, when S < 0.6 m/m, a significant fraction of pixels diverges from the 1:1 trend. A majority of pixels have a hydraulic slope S_h lower than S in the river where the water depth is higher than the topographic roughness resulting in a smoother water surface. This results in a hydraulic slope with a mean of 0.04 m/m

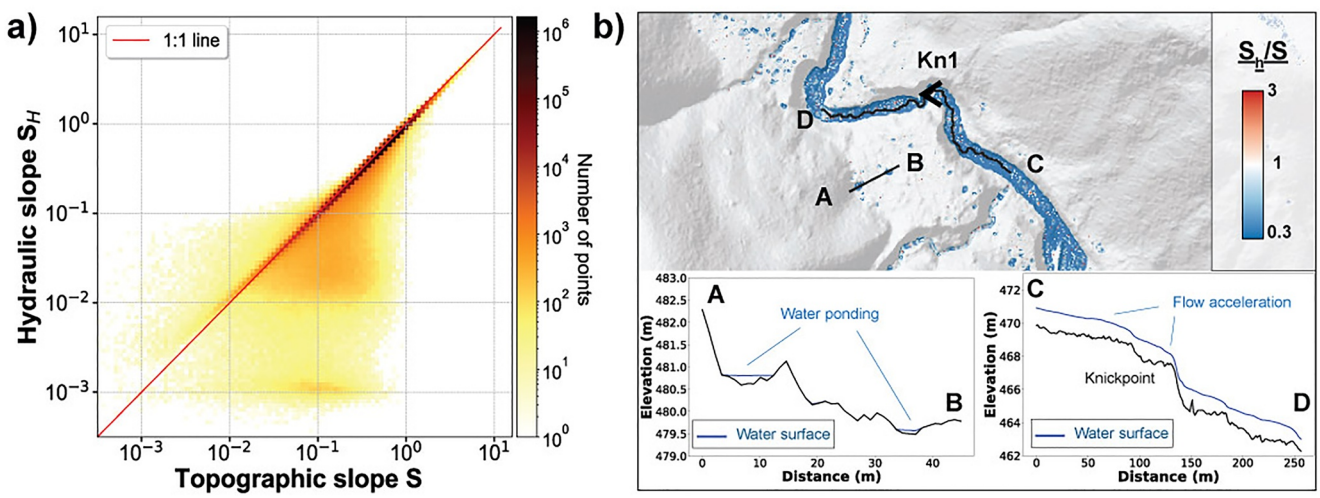

Figure 5. Comparison between the hydraulic slope S_h and the topographic slope S. (a) 2D histogram of S_h versus S. The number of bins in x and y axis is 100. (b) Subset of the Elder Creek catchment near knickpoint Kn1, showing the ratio between the two variables. Two cross sections show both situations where hydraulic slope is lower than topographic slope and vice versa.

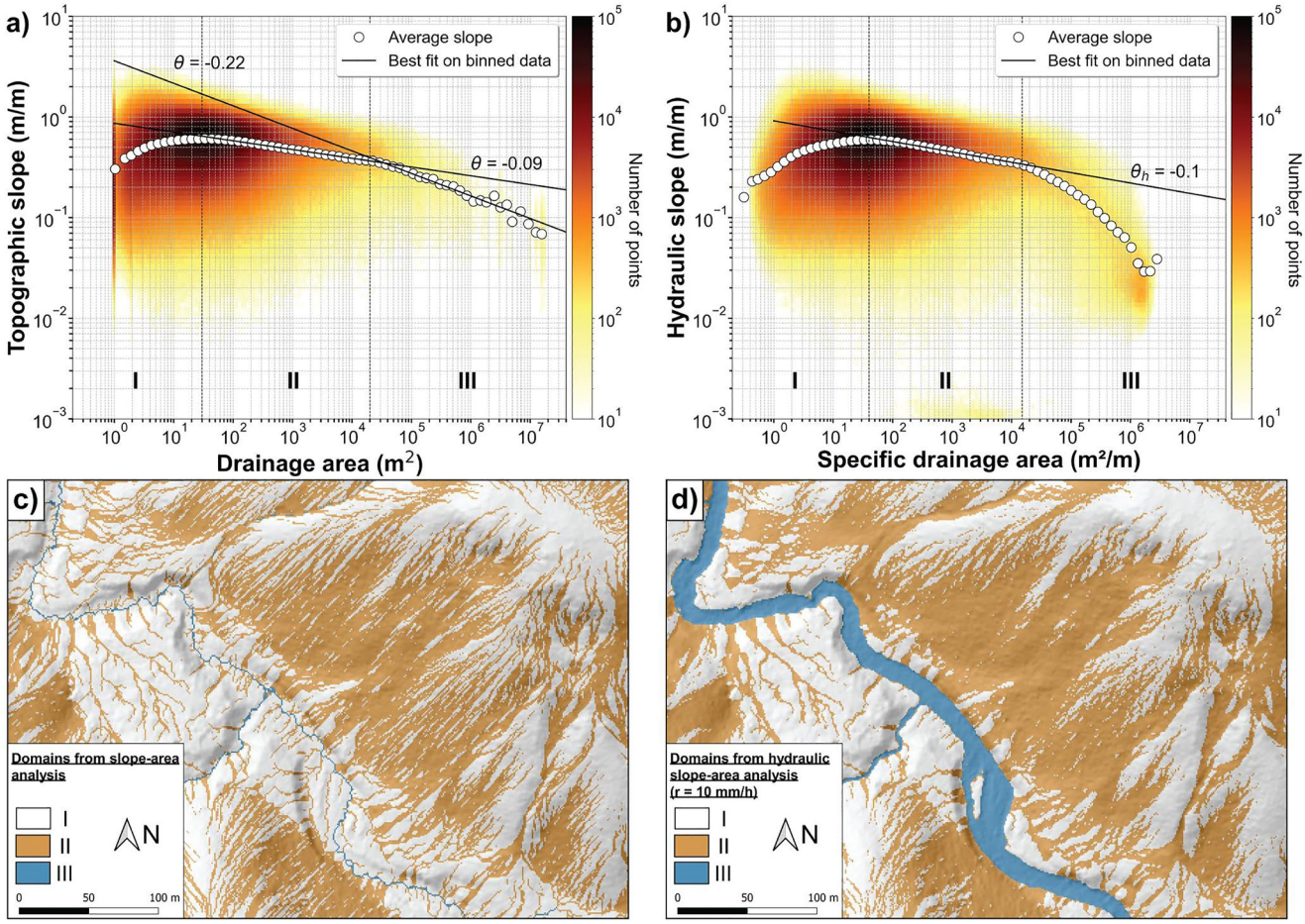

Figure 6. 2D density plot of (a) the traditional slope-area relationship and (b) the new hydraulic slope-area of the Elder Creek catchment. The hydraulic slope and specific drainage area are computed for $r = 10$ mm/hr. (c) Geomorphic domains classified by the slope-area approach. (d) Geomorphic domains classified by the hydraulic slope-area approach.

nearly three times smaller than the mean topographic slope (0.11 m/m, Figure S2 in Supporting Information S1). Similarly, the standard deviation of the hydraulic slope in the river is 45% smaller than the topographic slope (0.05 m/m vs. 0.09 m/m) highlighting the smoothing effect on the water surface. As shown in Davy et al. (2017), the precipiton solution deals adequately with closed depressions of any size, either related to true features of the topography (ponds, lakes) or DEM errors (Figure 5b). Water fills and overtops the depression resulting in a nearly flat hydraulic surface where the slope equals the height of the precipitons (at 1 m resolution), corresponding in this simulation to a minimum resolving slope of $S_h = 10^{-3}$ m/m. A smaller fraction of pixels shows cases where S_h is higher than S. These correspond to non-uniform flow conditions upstream of knickpoints (flow acceleration, Figure 5b) and immediately downstream (flow deceleration). Hence, while hydraulic and topographic slopes are similar on steep hillslopes, major differences occurs in low slope area corresponding to channels and floodplains, where the hydraulic model is much less influenced by small scale roughness that is known to severely affect local topographic slope measurement (Perron & Royden, 2013).

3.2. A Consistent Slope-Area Diagram for Landscape Analysis With Wide Rivers

3.2.1. The Hydraulic Slope-Area Diagram

Figure 6a illustrates the 2D density plot of the slope-area (S-A) diagram of the Elder Creek catchment computed from the 1 m LiDAR DEM. In Figure 6b, we introduce what we call the hydraulic slope-area (S_h-a_s) diagram that relates the hydraulic slope S_h with the specific drainage area a_s. Built on the legacy of the S-A relationship, we aim

to explore the ability of this diagram to identify geomorphic process domains in comparison to the *S-A* diagram. To reduce the scatter of both plots, slopes are averaged according to a logarithmic binning of a_s or A.

The mean *S-A* relationship exhibits three different trends in a log-log space (Figure 6a). We identify the transition between each trend as a critical drainage area by analyzing the plot derivative ($\delta S/\delta A$; Vergari et al., 2019; Figure S3 in Supporting Information S1). Following the partitioning of Montgomery and Foufoula-Georgiou (1993), the *S-A* diagram can be divided in three domains defined between two different trends. In domain I, the mean *S-A* relationship has a positive gradient ($\delta S/\delta A > 0$). The transition toward domain II occurs for $A = 30$ m^2 where the *S-A* scaling becomes negative ($\delta S/\delta A < 0$) following a power-law relationship of the form of Equation 1 with an exponent $\theta = -0.09 \pm 0.001$. The domain III begins at $A = 2 \times 10^4$ m^2 until the maximum drainage area of 2×10^7 m^2 within which the *S-A* power law scaling relationship exhibits an exponent $\theta = -0.22 \pm 0.007$.

To the first order, the mean S_h-a_s relationship also exhibits three different trends defining three domains (Figure 6b). Similarly to the *S-A* diagram, the transition between each trend is defined as a critical specific drainage area using the plot derivative ($\delta S_h/\delta a_s$). In domain I and II, the mean S_h-a_s relationship shows a similar trend than the mean *S-A* relationship. The transition between the two domains is at $a_s = 40$ m^2/m slightly higher than the critical drainage area in the *S-A* diagram. The S_h-a_s scaling in domain II follows a negative power-law relationship of the form:

$$S_h = k_h a_s^{-\theta_h} \tag{9}$$

where k_h can be defined as the hydraulic steepness index and θ_h the hydraulic concavity index. The S_h-a_s scaling exponent is $\theta_h = -0.10 \pm 0.002$ (Equation 9) and is nearly equal to θ in the *S-A* diagram. A patch of pixels characterized by low hydraulic slopes ($S_h < 10^{-2}$ m/m) is visible in domain II that is not present in the *S-A* diagram. These pixels correspond to very flat water surfaces (e.g., lakes, water pools etc.) where the slope is set by the precipiton height. The transition from domain II to III occurs around $a_s = 1.5 \times 10^4$ m^2/m. However, in domain III, the mean S_h-a_s relationship shows a steeper gradient than the *S-A* relationship, leading to a sharper transition between domain II and III. The S_h-a_s trend does not exhibit a single power-law behavior. Rather, the S_h-a_s relationship trend slightly varies toward a steeper gradient around 10^5 m^2/m. Above $a_s \sim 2 \times 10^6$ m^2/m, the mean hydraulic slope slightly increases until the maximum value of $a_s = 4 \times 10^6$ m^2/m is reached.

Figures 6c and 6d show domains I, II and III defined by the *S-A* and S_h-a_s approaches, respectively. Domain I and II correlate mostly with the presence of convex hillslopes and concave unchanneled valleys (Montgomery & Foufoula-Georgiou, 1993). The domain II defined by the S_h-a_s is spatially more continuous than the domain II defined by the *S-A* approach, owing to the spreading of the water surface. In both cases, the domain III is associated to the channel network. Yet, the extent and shape are very different. The number of pixels in the domain III defined by the S_h-a_s approach is nearly three times higher than with the *S-A* approach as shown in Figure 6b; and the distribution of a_s in this domain is much more continuous than the drainage area. Figure 6d shows that, as expected, the domain III identified by the S_h-a_s approach accurately captures the true extent of the channel. Figure 7a maps in the *S-A* diagram the location of pixels identified as the fluvial domain by the S_h-a_s approach (Figure 7b). These pixels incorrectly plot in the domain I or II in the *S-A* diagram (Figures 6c and 7a) and are thus wrongly considered as hillslopes and unchanneled valleys with traditional flow routing algorithms.

3.2.2. Sensitivity to the DEM Resolution

We perform D∞ topographic analysis and hydraulic simulations on 1, 2, 4, and 10 m DEM resolutions using a runoff rate of 10 mm/hr. Figure 8 presents the mean *S-A* and S_h-a_s relationships for the various pixel sizes. The pixel size has been increased from the 1 m DEM by considering the mean elevation in a sliding window of the size equal to the expected final resolution.

In the *S-A* diagram, the three domains are visible for the 1, 2, 4, and 10 m DEMs (Figure 8a). However, the critical drainage area (A_c) between domain I and II strongly varies according to the grid cell size from 40 to 400 m^2 for 1 and 10 m DEM resolution respectively. In domain III, the mean *S-A* scaling relationship is insensitive to the pixel size except for 1 m for which the topographic slope is higher for $A > 10^6$ m^2. Dividing the drainage area by the pixel size allows to reduce the pixel size effect around the transition from domain I to II but inevitably transfers this effect in domain III (Figure S4 in Supporting Information S1).

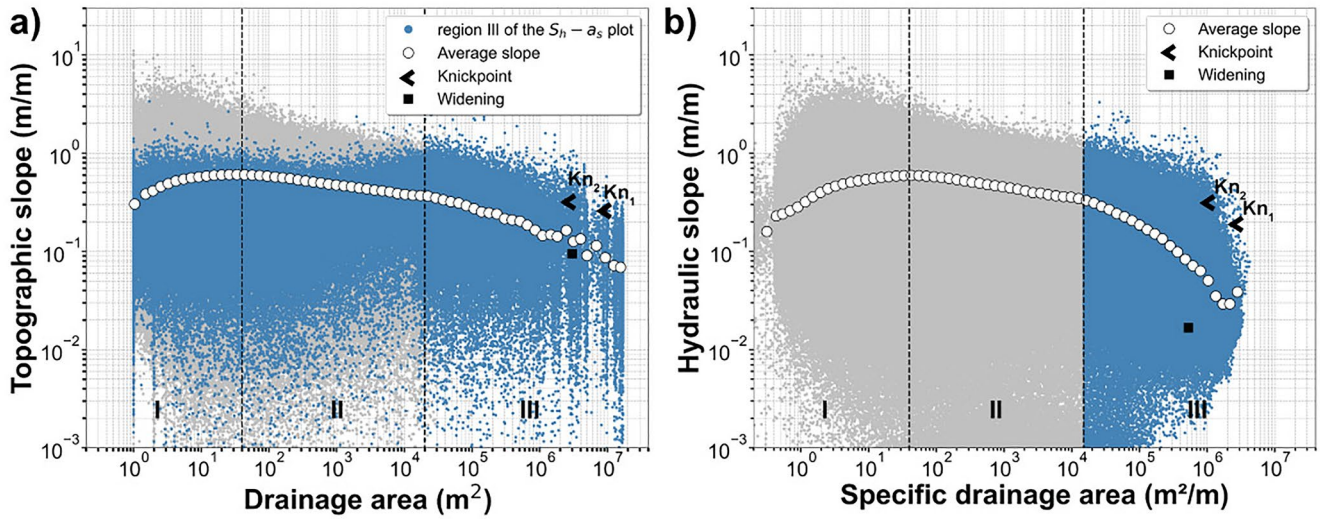

Figure 7. (a) Slope-area and (b) hydraulic slope-area diagrams with blue points representing pixels located in domain III of the hydraulic slope-area diagram (Figure 6b). Black arrows represent the average slope and specific drainage area or drainage area for the two knickpoints Kn1 and Kn2 (Figure 2). The black square represents a channel widening upstream of Kn2.

Unlike the *S-A* diagram, the critical specific drainage area defining the transition from domain I to II does not vary according to the pixel size in the S_h-a_s diagram (Figure 8b). It can also be observed that the mean S_h-a_s trend gradient in domain I decreases with the pixel size. While the transition from domain II to III is well defined for 1, 2, and 4 m DEM resolutions, it does not appear for the 10 m DEM. However, as observed in Figures 6 and 7, the inflexion point around $a_s = 2 \times 10^5$ m^2/m is still visible. Apart from domain I, the S_h-a_s mean relationship described for pixel sizes of 1, 2, and 4 m is very similar.

3.2.3. Multi-Runoff Analysis of the Hydraulic Slope-Area Diagram

While there can only be one calculation of D8 or D∞ based on topography, water depth can be predicted for various runoff intensities r. Both the hydraulic slope and the specific drainage area are expected to vary locally as a function of r leading to changes in the S_h-a_s diagram. Therefore, we adopt the notation S_h-$a_s(r)$ to specify the runoff rate for which the hydraulic slope-area analysis is performed. In what follows, we perform three simulations using different runoff rates representing low flow conditions (1 mm/hr), high flow conditions (10 mm/hr)

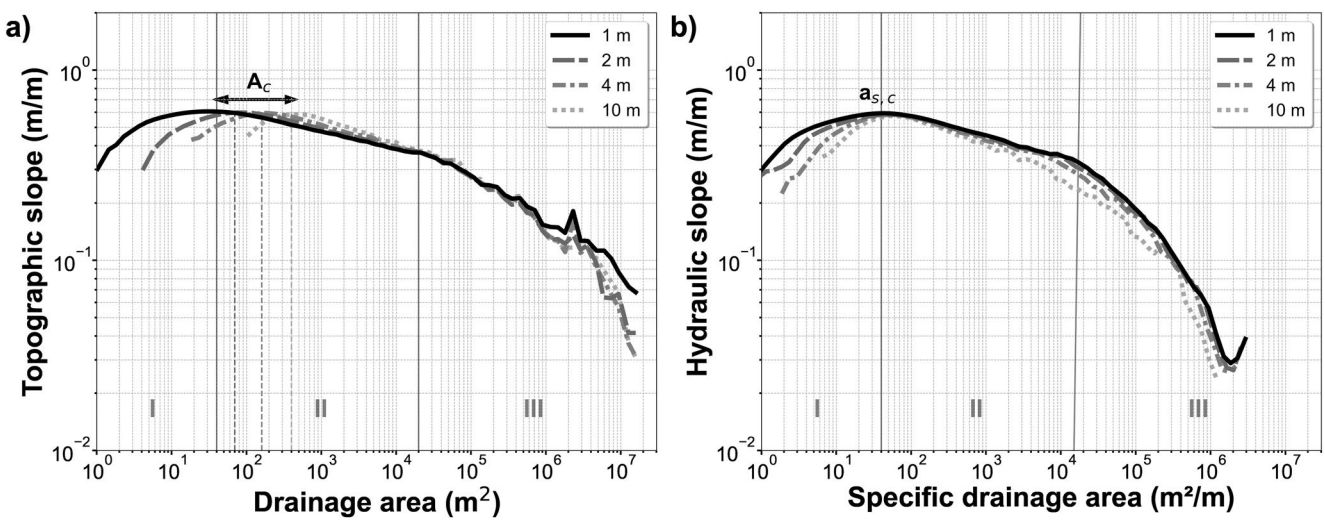

Figure 8. Effect of the pixel size on the mean (a) *S-A* and (b) S_h-a_s trends. Curved lines represent the average slope for the given a_s or A log interval. Vertical lines highlight the critical specific drainage area ($a_{s,c}$) or drainage area (A_c) between two domains according to the given grid cell size.

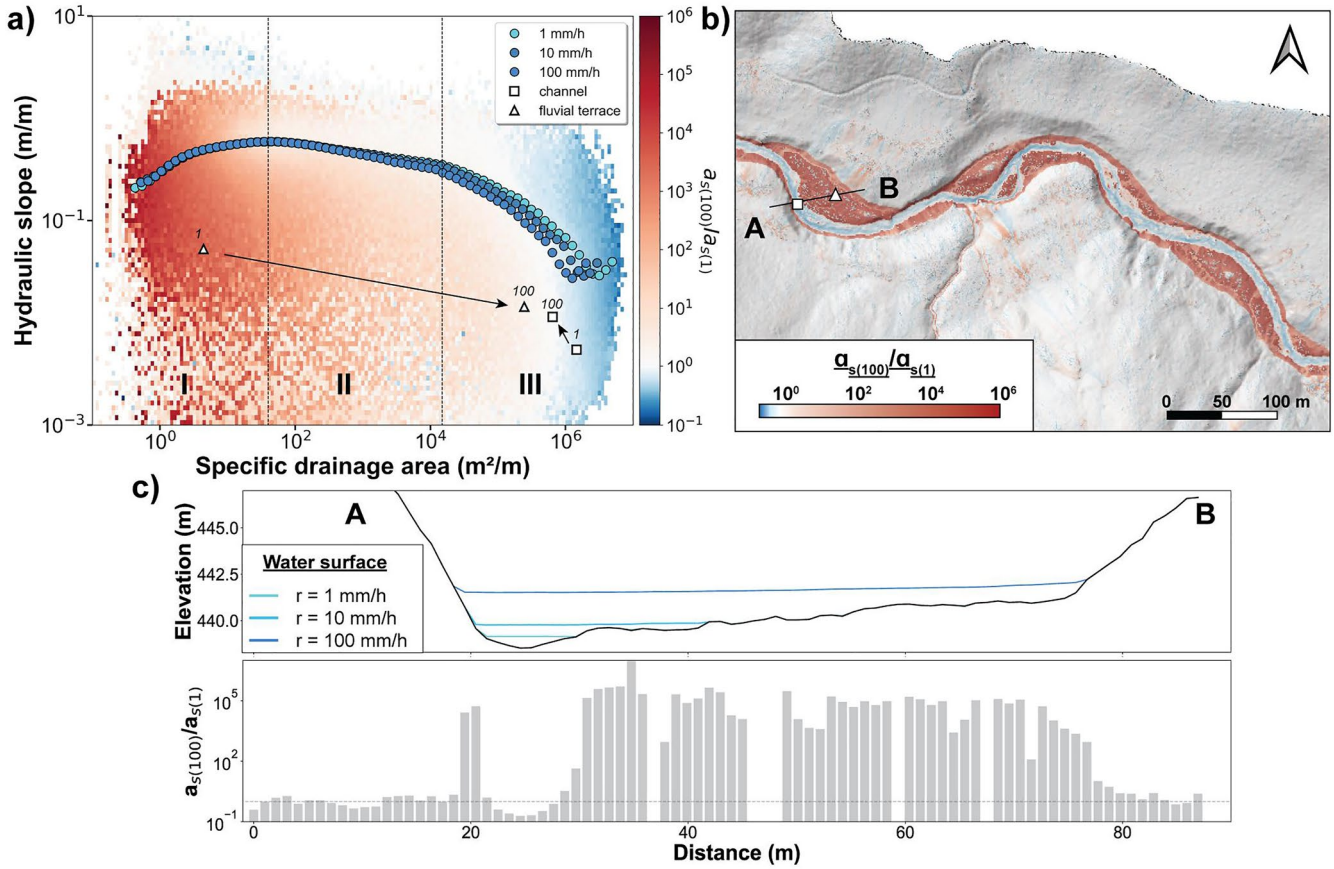

Figure 9. Multi-runoff analysis of the S_h-a_s diagram. (a) 2D histogram of the hydraulic slope-area relationship for $r = 1$ mm/hr. The color scale represents the ratio between the specific drainage at a runoff rate of 100 mm/hr ($a_s(100)$) and 1 mm/hr ($a_s(1)$) measured on the same pixel. White squares and triangles represents the mean a_s and S_h values of the channel and the floodplain, respectively, along the cross-section A-B (Figure 9b) for runoff rates of 1 mm/hr and 100 mm/hr. (b) Map of the $a_{s(100)}/a_{s(1)}$ ratio. Location of this map in the Elder Creek catchment is shown in Figure 13. (c) Cross-section of the A-B profile in (b) showing the water surface for different runoff rates together with the $a_{s(100)}/a_{s(1)}$ ratio. The horizontal dashed-line is set to $a_{s(100)}/a_{s(1)} = 1$. Note the log-log scale for the $a_{s(100)}/a_{s(1)}$ ratio in the above figures.

and a flash flood event (100 mm/hr). The specific drainage area is then calculated for each runoff rate. Each pixel thus supports a hydraulic slope and specific drainage area information for each input r which allows to analyze their variations by defining, for instance, ratios between two r.

The resulting S_h-$a_s(1,10,100)$ diagrams show that the variation in specific drainage area is up to five orders of magnitude between $r = 1$ and $r = 100$ mm/hr (Figure 9a). Therefore, we focus our analysis on the ratio between $a_{s(100)}$ and $a_{s(1)}$ ($a_{s(100)}/a_{s(1)}$ ratio) that maximizes the variation of the specific drainage area to better illustrate the dependency of this hydro-geomorphic metric to the runoff rate (Figure 9).

Figure 9a shows that the mean S_h-a_s trends of domain I and II are largely insensitive to the runoff rate. However, in domain III, the gradient of the mean S_h-a_s trend increases with r. A map of the $a_{s(100)}/a_{s(1)}$ ratio (Figure 9b) shows that this ratio is close to 1 in the vast majority of the landscape corresponding to domains I and II, explaining the stability of the mean S_h-a_s relationship. In these domains, flow patterns barely change with runoff, such that unit discharge varies in proportion of runoff and a_s is independent of r (Equation 6). On the contrary, overbank flow occurring as r increases (Figure 9c) significantly changes flow patterns and flow width in the vicinity of channels. The resulting pattern of the $a_{s(100)}/a_{s(1)}$ ratio is a decrease below unity in the deepest part of channels, and a massive increase on floodplains inundated for $r = 100$ mm/hr (Figures 9b and 9c). The decrease of a_s with r in the deepest part of channels is related to a more rapid increase of flow width with overbank flow than unit discharge (Equation 5). On the contrary, a_s increases extremely rapidly with r the moment an overbank pixel becomes flooded. In the S_h-a_s diagram, pixels located on floodplains thus plot in domain I or II at low runoff rate but plot in domain III when flooded (Figure 9a). This is illustrated by the white triangles in Figure 9a which represent

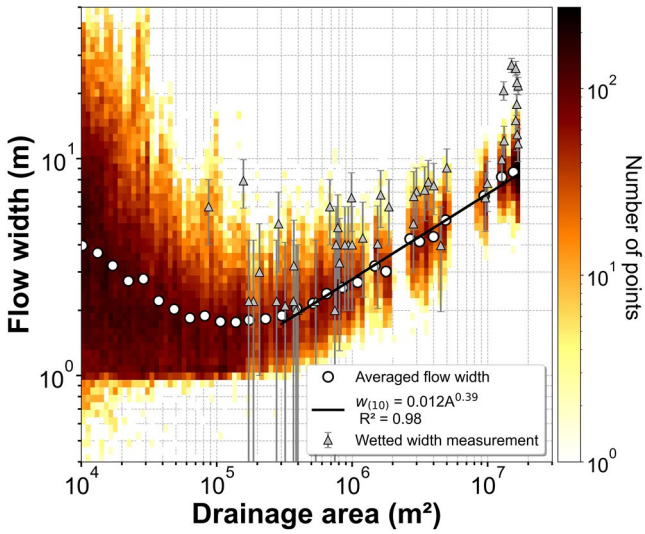

Figure 10. 2D histogram of flow width versus drainage area for a runoff rate $r = 10$ mm/hr and the wetted width versus drainage area. The drainage area A values were calculated with a D8 flow algorithm applied to the specific discharge map where $A \geq 10^4$ m^2. The best fit is estimated on binned data.

the mean S_h and a_s for the floodplain section in Figure 9c. Here, the specific drainage area increases by five orders of magnitude while the hydraulic slope decreases by less than one order of magnitude. On the same Figure, white square correspond to the mean S_h and a_s for $r = 1$ mm/hr and $r = 100$ mm/hr along the channel section (Figure 9c) and exhibit a 50% reduction of a_s and a two-fold increase of S_h with r.

3.3. Scaling of the Effective Flow Width

3.3.1. Effective Flow Width Versus Drainage Area

In bedrock rivers, channel flow width W has been shown to scale with drainage area as:

$$W = k_w A^b \tag{10}$$

where k_w is the width index and b the width-area scaling exponent typically of the order of 0.35 ± 0.11 for channels smaller than 10 m, a size similar to the Elder Creek channels (Lague, 2014; Montgomery & Gran, 2001; Snyder et al., 2003; Yanites et al., 2010). Here, we calculate the effective flow width at $r = 10$ mm/hr from $A > 10^4$ m^2 corresponding to the transition from domain II to III in the S-A diagram (Figure 6a). Figure 10 shows the relation between $w(r)$ and A, as there can only be one measurement of effective channel width for a given cross section. Figure 10 shows that above 3×10^5 m^2, $w(r)$ increases with A as a power-law of the form of Equation 10. A fit to the log-binned data shows that $k_w = 0.012 \pm 0.09$ and $b = 0.39 \pm 0.01$ ($R^2 = 0.98$). A comparison of $w(r)$ to the wetted width measured on the simulation result, equivalent to the width that would be measured on aerial imagery, shows that they exhibit a similar trend, albeit with a higher value of the wetted width owing to our definition of the effective channel width. However, the systematic evaluation of channel width at each pixel along the drainage network results in a more robust mean trend than what could be inferred from the wetted width measurements. Because the effective width is a continuous measure, the power-law scaling also extend continuously down to $A \sim 3 \times 10^5$ m^2 and a mean effective width of 2 m. On the contrary, below $A < 10^6$ m^2, no clear power-law trend can be detected on wetted width values, a limit that may be related to the discretization effect occurring when measuring small flow width on a 1 m DEM.

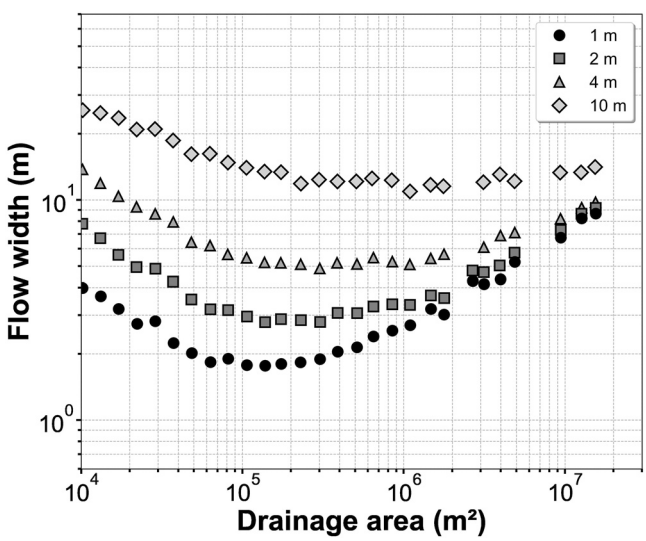

Figure 11. Flow width versus drainage area in function of the DEM resolution for a runoff rate $r = 10$ mm/hr.

For $A < 3 \times 10^5$ m^2, $w(r)$ exhibits a strong scatter with values ranging between 1 and 40 m for a single drainage area that we interpret as a breakdown of our assumption of a channelized flow. We further explore this hypothesis by testing the sensitivity of the mean $w(r)$-A relationship to the DEM resolution.

3.3.2. Sensitivity to the DEM Resolution

Figure 11 shows the mean $w(r)$-A relationship for a pixel size of 1, 2, 4, and 10 m with $w(r)$ estimated with $r = 10$ mm/hr. First, the results show that, for a given drainage area, $w(r)$ varies according to the pixel size. For instance, for $A = 10^5$ m^2, the mean $w(r)$ is equal to 2, 3, 5, and 14 m for a pixel size of 1, 2, 4, and 10 m, respectively. However, it can be observed that this pixel size effect decreases with increasing A where the mean $w(r)$ converges to 10 m at $A = 1.5 \times 10^7$ m^2 for all pixel sizes but 10 m. Comparison of the relationship between the 1 and 2 m DEM shows that the relationship are similar down to an effective width of 4 m. Hence, the effective width measure appears to be robust to DEM resolution as long as it about twice the pixel size. Consequently, at 10 m pixel size, the river channel geometry, characterized by a maximum width of 15 m measured from the 1 m DEM, cannot be fully described and no power-law scaling is observed for $A > 2 \times 10^5$ m^2. We note that the area below which the mean channel width decreases with A is

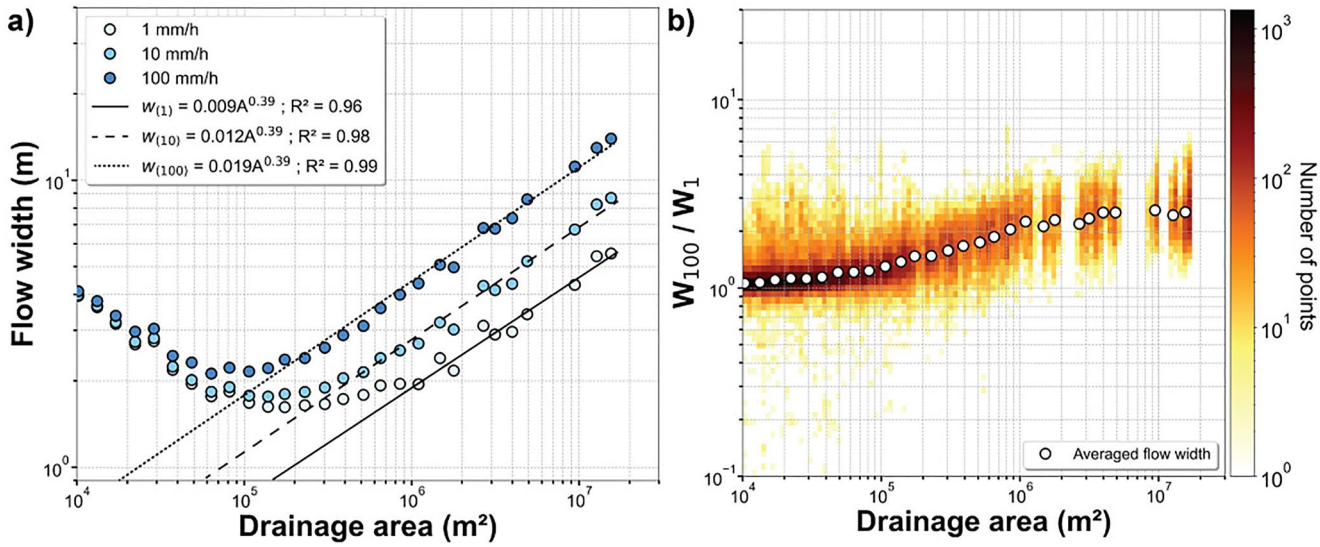

Figure 12. Multi-runoff analysis of the flow width versus drainage area relationship. (a) $w(r)$-A for runoff intensities of 1, 10, and 100 mm/hr. Linear models are applied above a critical drainage area depending on the runoff rate r. For r equals to 1, 10, and 100 mm/hr, the critical drainage area is 10^6, 3×10^5, and 1×10^5 m^2 respectively. (b) 2D histogram of the ratio between the flow width at 100 and 1 mm/hr ($w_{(100)}/w_{(1)}$ ratio) versus drainage area.

rather constant at $\sim 10^5$ for all DEM resolutions pointing to an effect related to flow patterns occurring at a scale larger than 10 m.

3.3.3. Multi-Runoff Analysis

The variation of the flow width at a given location for different runoff intensities is one element of the at-a-station hydraulic geometry (Leopold & Maddock, 1953). Given that $w(r)$ depends on r (Equation 8), we hereafter analyze the $w(r)$-A relationship for runoff rates equal to 1, 10, and 100 mm/hr (Figure 12).

Results show that the mean $w(r)$-A trends are insensitive to the runoff rate for $10^4 \leqslant A < 10^5$ m^2. Above 10^5 m^2, the mean $w(r)$ increases with A, following a power law relationship of the form of Equation 10 with the same exponent $b = 0.39$, but with a width index k_w increasing with r (Figure 12a, $k_w = 0.009$ for $r = 10$ mm/hr to $k_w = 0.019$ for $r = 100$ mm/hr). While the power law behavior can be observed from $A = 2 \times 10^5$ m^2 to $A = 3 \times 10^5$ m^2 for a runoff rate of 10 and 100 mm/hr respectively, this behavior only occurs at $A = 10^6$ m^2 for $r = 1$ mm/hr where the mean $w(r)$ is equal to twice the pixel size.

As explained in Section 3.1.2., $w(r)$ can be defined for various runoff rates for a given pixel allowing the definition of $w(r)$ ratios between two different input runoff rates. Here we explore how this ratio could be a metric of the alongstream change of hydraulic geometry using the two extreme runoffs 1 mm/hr and 100 mm/hr (Figure 12b). For $A < 10^5$ m^2, and as expected from Figure 12a, the $w_{(100)}/w_{(1)}$ ratio is close to 1. As for the $a_{s(100)}/a_{s(1)}$ ratio in domain I and II, this means that flow accumulation patterns and the resulting $a_s(r)$ are similar whatever the runoff. For $10^5 \leq A < 10^6$ m^2, the $w_{(100)}/w_{(1)}$ ratio increases up to a value of 2.5 that remains about constant for $A > 10^6$ m^2. This tendency can be interpreted as a downstream variation in the channel hydraulic geometry starting from narrow confined channel with limited width variation with discharge, to more concave channels with more pronounced overbank flow with increasing runoff. But the increase in $w_{(100)}/w_{(1)}$ ratio could also be related to a DEM resolution effect for which effective widths smaller than 2 m are not properly resolved. Whatever the cause, for $A \geq 10^6$ m^2, the mean constant $w_{(100)}/w_{(1)}$ ratio shows that the at-a-station channel geometry is independent of drainage area on average, although individual data points show a range between 1.5 and up to 6.

4. Discussion

Given the objectives of this paper, the complexity of the 2D hydraulic simulation approach is intentionally reduced to a uniform runoff rate and friction coefficient (Section 2.3). The main idea is to obtain a consistent flow routing able to fully capture the geometric complexity of geomorphic systems when they are described at fine scale as

allowed by high resolution LiDAR data. However, this approach can also be useful in channel analyses for any DEM resolution where channels are much larger than the pixel size (e.g. ALOS Palsar, SRTM, TanDEM-X etc.). Although in this paper we do not discuss the quality of the data we use, we are aware of some limitations related to the use of airborne lidar topographies related to the lack of actual bathymetric measurement in flooded areas (e.g., Lague & Feldmann, 2020). Also, although the quantification of the uncertainty associated to each metric has not been considered, it may help to confidently evaluate the accuracy related to each measurement in future studies. However, as this study is mainly focused in the identification of geomorphic transitions, we expect that the variability of the landscape structure within the catchment, due to the variability in lithological and tectonic conditions, is the primary factor controlling the location of geomorphic transitions rather than the uncertainty associated to each metric (e.g., Clubb et al., 2019; Ramsey et al., 2006; Vergari et al., 2019).

4.1. A New Set of 2D Hydro-Geomorphic Metrics

The use of 2D SWEs modeling allows the direct integration of flow width in the calculation of the specific drainage area and allows its application to the river network. In comparison to the traditional drainage area A, the specific drainage area gives a better description of the entire flooded section of the channel (Figure 3b). However, a_s does not have the same hierarchical behavior than A. While A only increases downstream, a_s both increases downstream at the catchment scale and laterally along the channel section toward the center of the channel (i.e., where the flow is maximum). The sensitivity analyses to the DEM resolution also show different dependencies on the pixel size between a_s and A. While A is sensitive to the DEM resolution on hillslopes, where the flow is not channelized, it is not in channel environment (Figure 8a). The specific drainage area does not depend on the pixel size on hillslopes and in channel environment as long as the river width is larger than the pixel size (Figure 8b). For channels narrower than the pixel size, the specific drainage area is set by the DEM resolution.

Channel width is a crucial hydraulic variable as it is used in the calculation of the bed shear stress that controls the river's response to tectonic, climatic and lithological conditions (Baynes et al., 2018; Croissant et al., 2017; Lague, 2014; Whipple, 2004; Whipple et al., 2013; Wobus et al., 2006). It is essential to quantify unit discharge (Leopold & Maddock, 1953), sediment-transport capacity (Croissant et al., 2019; Davy et al., 2017), and bedrock incision rate (Finnegan et al., 2007; Lague, 2014; Whipple et al., 2013; Wobus et al., 2006; Yanites, 2018; Yanites et al., 2010). By considering both total drainage area and the specific area, we show that it is possible to calculate a proxy for the flow width $w(r)$ for a given runoff rate. $w(r)$ does not formally give the water extent, in contrast to previous method based on aerial or satellite imagery (Fisher et al., 2013; Güneralp et al., 2014; Pavelsky & Smith, 2008; Rowland et al., 2016; Schwenk et al., 2017), but it represents an effective width where most of the flow occurs for a given discharge. It also differs from previous DEM-based methodologies for which the channel width is measured from the elevation of the top or the toe of the channel banks following a statistical threshold approach from topographic features (Johansen et al., 2011; Passalacqua et al., 2012; Sofia et al., 2015). Thanks to the ability of Floodos to represent any river morphology (i.e., straight, braided, meander or braided rivers) without having to define a priori the wet and dry zones (Davy et al., 2017), $w(r)$ can be calculated for any channel type and for various discharges in order to describe the at-a-station hydraulic geometry (Leopold & Maddock, 1953). It is also a continuous measure and as such is less prone to discretization effects related to grid resolution (Figure 10). Obviously, the DEM resolution must be sufficiently fine to obtain a relevant measurement of the flow width (see Figure 11). Even though further comparisons with field measurements are needed, we illustrate here the potential of using 2D hydraulic simulation to provide channel width estimations in a relatively simple and straightforward way. This provides new opportunities to systematically analyze downstream and at-a-station variations of the channel width in relation to climatic and tectonic perturbations in future studies.

We show that as the topographic slope is sensitive to the DEM roughness, this measure overestimates the channel slope. Nonetheless, the topographic slope measured from traditional flow algorithms affected by the DEM roughness may still differ from the reach slope relevant to flow dynamics (Perron & Royden, 2013; Figure 1). We show that this limitation can be overcome by measuring the hydraulic slope resulting from the flow dynamic simulated by the 2D SWEs model. As the hydraulic slope is measured from the water surface, it is (a) less affected by the DEM roughness issue than the topographic slope if the water depth is larger than this roughness and (b) relevant to any prediction related to flow including bedrock erosion or sediment transport.

4.2. Identification of Hillslope-Channel Connexions Using the Hydraulic Slope-Area Diagram

In this study, we highlight the limitations of using the *S-A* approach to identify geomorphic domains from HRDEM. We demonstrate that this representation is biased by the inability of the D∞ flow routing algorithm to correctly capture flow accumulation patterns within river channels spanning several pixels wide. This leads to artificially low drainage areas in all pixels of a channel cross-section but one where drainage area concentrates. In the *S-A* diagram, a large area of the channel network thus plots in domain I and II and is incorrectly identified as hillslopes or unchanneled valleys, underestimating the extent of the channel network. In the Elder Creek catchment, using $r = 10$ mm/hr, up to 2/3 of the channel network is missing with a D∞ classification approach. In the same way, the extent of hillslopes and valleys is overestimated.

On the other hand, the structure of the S_h-a_s diagram is more consistent with the identification of the fluvial system since all flooded channel sections are characterized by a high specific drainage area and thus plot in domain III as expected. In addition, we show that the hillslope-to-valley transition is sensitive to the DEM resolution in the *S-A* plot but insensitive in the S_h-a_s diagram (Figure 8). The accurate identification of domain transitions is of primary importance in the determination of the characteristic length of hillslopes for hydrological models (Montgomery & Foufoula-Georgiou, 1993) and to understand what control the valley spacing in natural environments (Perron et al., 2008).

4.3. Characterization of the River Morphology

4.3.1. The Effective Flow Width Versus Drainage Area

The ability to measure systematically the effective flow width $w(r)$ on the entire drainage network and its relation to the drainage area provides a new approach to extract synoptic measurements of channel width over the entire drainage network. In the Elder Creek catchment, we find that $w(r)$ varies on average with A as a power law with an exponent $b = 0.39$ consistent with values reported for bedrock rivers of similar size (Lague, 2014; Leopold & Maddock, 1953; Montgomery & Gran, 2001; Snyder et al., 2003; Whittaker et al., 2007; Yanites et al., 2010). This power-law scaling extends down to a range of area between 2×10^5 and 10^6 m^2, depending on the runoff rate, and where the mean effective width is equal to two pixels. We show that this area depends on the DEM resolution (Figure 11) such that we cannot decipher whether the departure from a power-law scaling indicates the emergence of channelization or is an effect of DEM resolution. Further analyses should be performed with finer DEM resolutions and ground truth checking to better understand the effective flow width versus drainage area relationship.

4.3.2. The Multi-Runoff Approach

We demonstrate a potential approach to characterize the morphology of the fluvial system which consists in analyzing the hydro-geomorphic metrics, the S_h-a_s diagram and the $w(r)$-A plot for multiple input runoff rates. The multi-runoff analysis shows that, in essence, the S_h-a_s and the $w(r)$-A diagrams are representative of flow conditions, which depend on rainfall conditions. A comparison of flow at different rainfall rates is an avenue to identify the geomorphic domains sensitive to the discharge, and to reveal hydraulic geometric properties of the channel network. Figure 13 illustrates for instance a classification of the Elder Creek catchment that combines the domains detected by the S_h-a_s at $r = 10$ mm/hr, enriched with multi-runoff features. On this map, floodplains are defined as parts of the landscape that are only flooded during large storm events and correspond to pixels with a ratio $a_{s(100)}/a_{s(1)}$ much larger than 1 (see Figure 13b, where points with $a_{s(100)}/a_{s(1)} > 10$ are colored in black). Figure 13b shows that this metric identifies the floodplain upstream of the knickpoint Kn2 formed by past debris flow deposition (Lovill et al., 2018; Seidl & Dietrich, 1992), while the *S-A* typology would have classified it as hillslope (Figure 13c). The ratio $w_{(100)}/w_{(1)}$ can be used to evaluate channel hydraulic geometry and can thus be used to identify domains where the hydraulic section is constrained (e.g., gorges) versus domains where it varies with flow (e.g., floodplain areas). Following Figure 12b, we separate reaches of the channel network for which the mean $w_{(100)}/w_{(1)}$ is greater than 2 occurring at $A = 10^6$ m^2 (Figure 13 in blue), thus building tools to quantify fluvial confinement which is expected to play a significant role in long-term sediment transport and incision (e.g., Croissant et al., 2019). More generally, by building for each pixel a vector of S_h and a_s for various runoffs, one can envision much richer automatic approaches to detect geomorphic domains and improve landscape analysis. Such analyses are beyond the capacity of the *S-A* method.

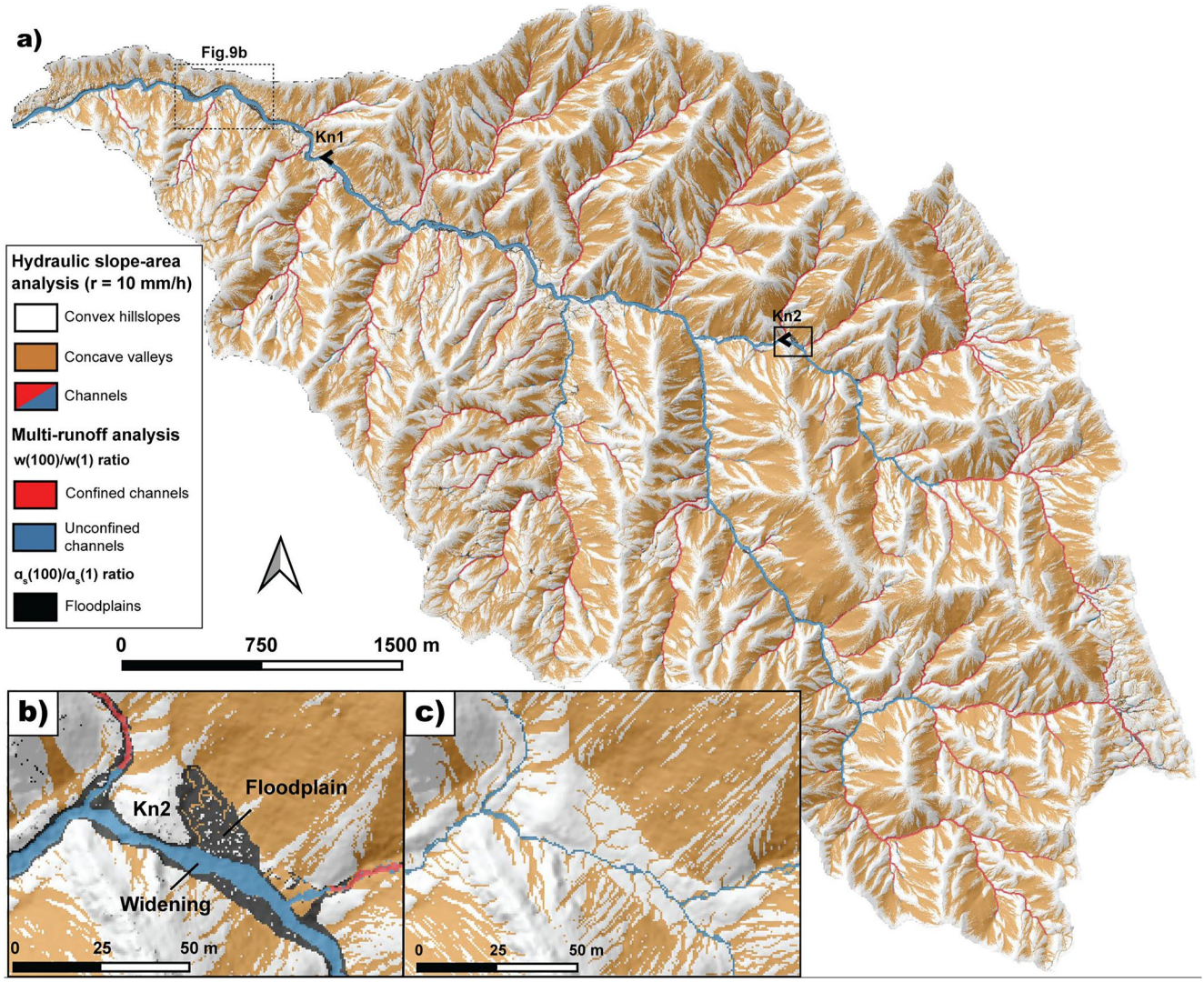

Figure 13. Map of the Elder Creek catchment showing geomorphic domains classified from the single runoff hydraulic slope-area (r = 10 mm/hr) and multi-runoff $w(r)$ and $a_s(r)$ analyses. (a) Overview of the Elder Creek catchment map. An operation of dilatation has been applied to the channel domain to increase the river segment width by a factor of 2. This operation has not been applied in (b and c). Pixels in blue and red belongs to the channel domain. (b) Focus on knickpoint Kn2 for which an upstream widening and floodplains are observed. (c) Same area as (b) classified from the slope-area analysis.

4.3.3. Potential of the Hydraulic Slope-Area Diagram for the Identification of Anomalous River Geometry

As described earlier, a_s varies according to both the local channel geometry and the position in the channel network. Therefore, the mean tendency between S_h and a_s hides local variations due to changes in both the hydraulic slope and/or flow width along the channel network that cannot be described using the *S-A* diagram. For instance, in slope-area diagrams, vertical step knickpoints are only characterized by a significantly higher slope that are recognized as spikes in the average trend (Goldrick & Bishop, 2007; Haviv et al., 2010; Whipple et al., 2013). This behavior can be observed in the *S-A* plot of the Elder Creek catchment where knickpoints Kn1 and Kn2 are present (Figure 7b). However, knickpoints not only modify local slope: they are also characterized by a narrowing of the channel (Baynes et al., 2018; Whittaker et al., 2007) and thus by an increase of a_s (Equation 5). Consequently, in the hydraulic slope-area diagram, knickpoints tend to be much more easily detected trough deviations from the mean trend owing to two factors: (a) first the hydraulic slope is less affected by DEM noise, allowing local slope anomalies to better stand out and (b) knickpoints are characterized by a combination of larger S_h and a_s than the average trend, which tends to enhance the detection capability compared to just a variation of

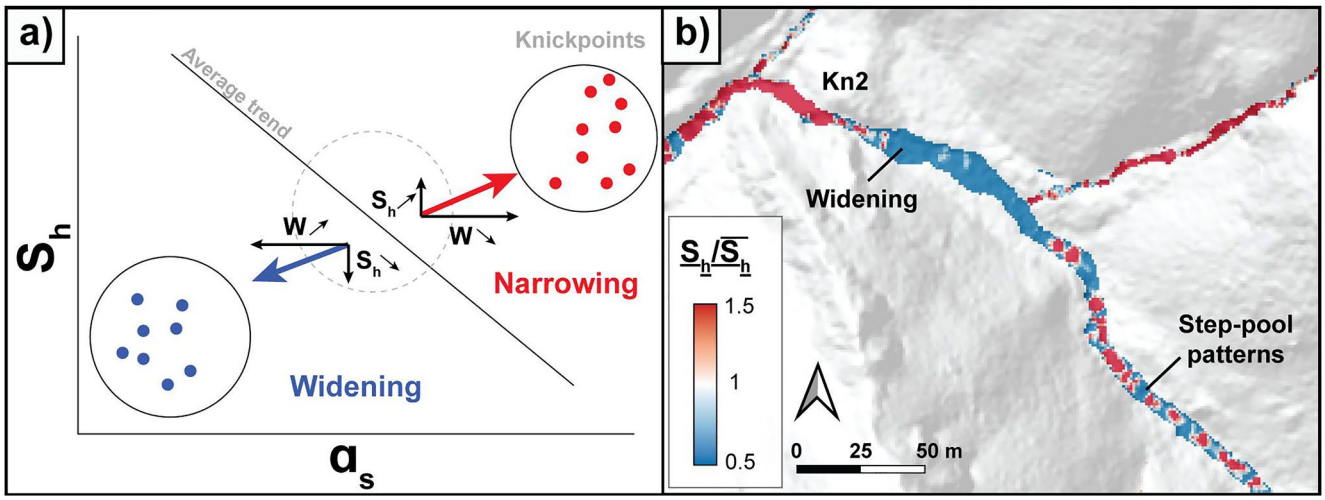

Figure 14. Potential detection of anomalous river geometry using the S_h-a_s diagram. (a) Sketch describing theoretical local variations of the specific drainage area and slope due to anomalous river geometry. (b) Map of the hydraulic slope to mean hydraulic slope ratio ($S_h/\bar{S}_h$), defined for $r = 10$ mm/hr, focusing on the knickpoint Kn2.

S. Conversely a widening of the channel has lower a_s and S_h than the average (Figure 14). For instance, the knickpoint Kn2 identified in Figure 13c is characterized by a channel narrowing and an upstream widening (Figure 7b). Both appear markedly apart from the mean S_h-a_s trend and are more easily detectable than in the *S*-*A* diagram (Figure 7a). Similary, the deviation from the mean S_h-a_s trend for the largest values of a_s corresponds to a log bin largely influenced by knickpoint Kn1 (Figures 6 and 7b) which exhibits a very pronounced narrowing and steepening. In the absence of a clear and unique power-law trend in the S_h-a_s relationship for the channel domain, we did not attempt to define an equivalent "steepness index" (Snyder et al., 2000; Wobus et al., 2006) for the S_h-a_s to produce steepness maps. However, a simple ratio of hydraulic slope to mean hydraulic slope for a given a_s bin provides a first order map of anomalies in the channel (Figure 14b) allowing detailed in channel features to be detected such as step-pool patterns. Compared to the *S*-*A* diagram, the S_h-a_s offers a greater sensitivity to detect transient channel geometries, and a richer way to describe channel patterns.

5. Conclusion

In this paper, we explored the added-value of 2D hydraulic simulations performed on high-resolution DEM to fluvial landscape analysis for which traditional flow routing algorithms fail to capture the fine structure of flow paths. We defined new metrics relying on the output parameters of the hydraulic simulations and used them to identify geomorphic domains. We applied the Floodos hydrodynamic model to the Elder Creek catchment, California, for which the river channel width (up to 15 m) is wider than the available 1-m LiDAR DEM. The model is applied with a constant and uniform runoff rate (r) assuming that runoff generation only results from the exceedance of infiltration capacity taken constant over the whole catchment. The main findings are the followings:

1. Hydro-geomorphic metrics consistent with a realistic flow pattern can be defined from the 2D hydraulic model. Among them, we define a normalized discharge per unit width equivalent to a specific drainage area (a_s). While this metric has been only defined on hillslopes in previous studies, its calculation is now extended to channels. Conversely to the classical drainage area, the specific drainage area directly integrates the 2D river structure geometry simulated by the model and thus varies downstream and according to transversal variations in the channel geometry. We propose an effective flow width parameter easily calculated from the ratio between the drainage area and the specific drainage area. This metric measures the width over which most of the flow occurs for a given runoff rate, and differs from the water surface extent. We also highlight the benefit of using the hydraulic slope (S_h) which is less affected by the DEM roughness than the topographic slope, more relevant to flow dynamics and can identify areas of non-uniform flow conditions (i.e., flow acceleration and deceleration).

2. Fluvial landscapes can be analyzed through relationships between the hydraulic slope and the specific drainage area (called the hydraulic slope-area (S_h-a_s) diagram) and the flow width with drainage area (the $w(r)$-A diagram). We demonstrate that the structure of the S_h-a_s diagram allows a better differentiation between hillslopes, unchanneled valleys and the channel network, with a reduced sensitivity to the DEM resolution than the S-A approach. It accurately captures the full extent of the channel network and the hillslope-channel connexions. The $w(r)$-A scaling relationship shows a power-law behavior with an exponent consistent with previous observations.
3. The ability to analyze the variations of the hydro-geomorphic metrics and the scaling relationships according to different runoff rates allows a richer description of the landscape organization. For instance, we used the $a_{s(100)}/a_{s(1)}$ ratio defined as the ratio between the specific drainage area computed for $r = 100$ and $r = 1$ mm/hr, respectively, to highlight discharge-dependent domains such as floodplains. In the same way, we use the $w_{(100)}/w_{(1)}$ characterizing at-a-station hydraulic geometry to identify confined and unconfined reaches along the channel network. Even though further development is needed, we show the potential of the multi-runoff approach in the characterization of the fluvial system.

This study provides additional arguments in favor of the use of 2D hydraulic simulation in combination with HRDEM to obtain a richer description of the landscape organization and channel geometry than traditional approaches. This approach is not limited to LiDAR HRDEMs and can also be useful when applied to lower DEM resolution where channels are wider than the pixel size. Application to other basins with different sizes and tectono-climatic conditions are needed to better define the ability of the present hydro-geomorphic metrics to identify important transitions between geomorphic processes, define universal behaviors and detect anomalies in landscape organization.

Data Availability Statement

Data supporting the results and the parameters used to perform the simulations are available in a FAIR data repository at (Bernard, 2021): https://doi.org/10.5281/zenodo.5721152. The version of Riverlab (and Floodos) used in this study can be accessed at https://doi.org/10.5281/zenodo.6037712 (Davy, 2022).

Acknowledgments
The authors wish to thank Philippe Steer and Edwin Baynes for their remarks and advices that helped improving this paper. This research has been supported by the Nantes-Rennes Topo-bathymetric LiDAR Platform of University Rennes 1, and by the Brittany Regional Council (Project LIDAREAU, Grant No. 2020-701). This research is also part of the PICS research project (https://pics.ifsttar.fr, last access: 28 May 2021) and has been supported by the Agence Nationale de la Recherche (Grant Nos. ANR-17-CE03-0011 and ANR eLabo ANR-17-LCV2-0012).

References

Arcement, G. J., & Schneider, V. R. (1989). Guide for selecting Manning's roughness coefficients for natural channels and flood plains. In *Area* (Vol. 2339). https://doi.org/10.3133/wsp2339

Bates, P. D., Horritt, M. S., & Fewtrell, T. J. (2010). A simple inertial formulation of the shallow water equations for efficient two-dimensional flood inundation modelling. *Journal of Hydrology*, *387*(1–2), 33–45. https://doi.org/10.1016/j.jhydrol.2010.03.027

Baynes, E. R. C., Lague, D., Attal, M., Gangloff, A., Kirstein, L. A., & Dugmore, A. J. (2018). River self-organisation inhibits discharge control on waterfall migration. *Scientific Reports*, *8*(1), 2444. https://doi.org/10.1038/s41598-018-20767-6

Bellos, V., & Tsakiris, G. (2016). A hybrid method for flood simulation in small catchments combining hydrodynamic and hydrological techniques. *Journal of Hydrology*, *540*, 331–339. https://doi.org/10.1016/j.jhydrol.2016.06.040

Bernard, T. (2021). Supporting dataset for the paper: "Hydro-geomorphic metrics for high resolution fluvial landscape analysis." Version 1 [Dataset]. Zenodo. https://doi.org/10.5281/zenodo.5721152

Beven, K. J., & Kirkby, M. J. (1979). A physically based, variable contributing area model of basin hydrology. *Hydrological Sciences Bulletin*, *24*(1), 43–69. https://doi.org/10.1080/02626667909491834

Booth, A. M., Roering, J. J., & Rempel, A. W. (2013). Topographic signatures and a general transport law for deep-seated landslides in a landscape evolution model. *Journal of Geophysical Research: Earth Surface*, *118*(2), 603–624. https://doi.org/10.1002/jgrf.20051

Bout, B., & Jetten, V. G. (2018). The validity of flow approximations when simulating catchment-integrated flash floods. *Journal of Hydrology*, *556*, 674–688. https://doi.org/10.1016/j.jhydrol.2017.11.033

Cea, L., Garrido, M., & Puertas, J. (2010). Experimental validation of two-dimensional depth-averaged models for forecasting rainfall–runoff from precipitation data in urban areas. *Journal of Hydrology*, *382*(1–4), 88–102. https://doi.org/10.1016/j.jhydrol.2009.12.020

Cea, L., Legout, C., Darboux, F., Esteves, M., & Nord, G. (2014). Experimental validation of a 2D overland flow model using high resolution water depth and velocity data. *Journal of Hydrology*, *513*, 142–153. https://doi.org/10.1016/j.jhydrol.2014.03.052

Clubb, F. J., Bookhagen, B., & Rheinwalt, A. (2019). Clustering river profiles to classify geomorphic domains. *Journal of Geophysical Research: Earth Surface*, *124*(6), 1417–1439. https://doi.org/10.1029/2019JF005025

Costabile, P., & Costanzo, C. (2021). A 2D-SWEs framework for efficient catchment-scale simulations: Hydrodynamic scaling properties of river networks and implications for non-uniform grids generation. *Journal of Hydrology*, *599*, 126306. https://doi.org/10.1016/j.jhydrol.2021.126306

Costabile, P., Costanzo, C., De Bartolo, S., Gangi, F., Macchione, F., & Tomasicchio, G. R. (2019). Hydraulic characterization of river networks based on flow patterns simulated by 2-D shallow water modeling: Scaling properties, multifractal interpretation, and perspectives for channel heads detection. *Water Resources Research*, *55*(9), 7717–7752. https://doi.org/10.1029/2018WR024083

Costabile, P., Costanzo, C., & Macchione, F. (2012). Comparative analysis of overland flow models using finite volume schemes. *Journal of Hydroinformatics*, *14*(1), 122–135. https://doi.org/10.2166/hydro.2011.077

Coulthard, T. J., Neal, J. C., Bates, P. D., Ramirez, J., de Almeida, G. A. M., & Hancock, G. R. (2013). Integrating the LISFLOOD-FP 2D hydrodynamic model with the CAESAR model: Implications for modelling landscape evolution. *Earth Surface Processes and Landforms*, *38*(15), 1897–1906. https://doi.org/10.1002/esp.3478

Crave, A., & Davy, P. (2001). A stochastic "precipiton" model for simulating erosion/sedimentation dynamics. *Computers and Geosciences*, *27*(7), 815–827. https://doi.org/10.1016/S0098-3004(00)00167-9

Croissant, T., Lague, D., & Davy, P. (2019). Channel widening downstream of valley gorges influenced by flood frequency and floodplain roughness. *Journal of Geophysical Research: Earth Surface*, *124*(1), 154–174. https://doi.org/10.1029/2018JF004767

Croissant, T., Lague, D., Steer, P., & Davy, P. (2017). Rapid post-seismic landslide evacuation boosted by dynamic river width. *Nature Geoscience*, *10*(9), 680–684. https://doi.org/10.1038/ngeo3005

David, A., & Schmalz, B. (2020). Flood hazard analysis in small catchments: Comparison of hydrological and hydrodynamic approaches by the use of direct rainfall. *Journal of Flood Risk Management*, *13*(4), 1–26. https://doi.org/10.1111/jfr3.12639

Davy, P. (2022). *Riverlab (version 6)*. https://doi.org/10.5281/zenodo.6037712

Davy, P., Croissant, T., & Lague, D. (2017). A precipiton method to calculate river hydrodynamics, with applications to flood prediction, landscape evolution models, and braiding instabilities. *Journal of Geophysical Research: Earth Surface*, *122*(8), 1491–1512. https://doi.org/10.1002/2016JF004156

Davy, P., & Lague, D. (2009). Fluvial erosion/transport equation of landscape evolution models revisited. *Journal of Geophysical Research: Solid Earth*, *114*(3), 1–16. https://doi.org/10.1029/2008JF001146

Dietrich, G. (2014). *Eel River Critical Zone Observatory July 2014 Lidar Survey*. https://doi.org/10.5069/G9MP517V

Finnegan, N. J., Sklar, L. S., & Fuller, T. K. (2007). Interplay of sediment supply, river incision, and channel morphology revealed by the transient evolution of an experimental bedrock channel. *Journal of Geophysical Research*, *112*(3), 1–17. https://doi.org/10.1029/2006JF000569

Fisher, G. B., Bookhagen, B., & Amos, C. B. (2013). Channel planform geometry and slopes from freely available high-spatial resolution imagery and DEM fusion: Implications for channel width scalings, erosion proxies, and fluvial signatures in tectonically active landscapes. *Geomorphology*, *194*, 46–56. https://doi.org/10.1016/j.geomorph.2013.04.011

Flint, J. J. (1974). Stream gradient as a function of order, magnitude, and discharge. *Water Resources Research*, *10*(5), 969–973. https://doi.org/10.1029/WR010i005p00969

Fuller, T. K., Perg, L. A., Willenbring, J. K., & Lepper, K. (2009). Field evidence for climate-driven changes in sediment supply leading to strath terrace formation. *Geology*, *37*(5), 467–470. https://doi.org/10.1130/G25487A.1

Gallant, J. C., & Hutchinson, M. F. (2011). A differential equation for specific catchment area. *Water Resources Research*, *47*(5), 1–14. https://doi.org/10.1029/2009WR008540

Goldrick, G., & Bishop, P. (2007). Regional analysis of bedrock stream long profiles: Evaluation of Hack's SL form, and formulation and assessment of an alternative (the DS form). *Earth Surface Processes and Landforms*, *32*(5), 649–671. https://doi.org/10.1002/esp.1413

Güneralp, I., Filippi, A. M., & Hales, B. (2014). Influence of river channel morphology and bank characteristics on water surface boundary delineation using high-resolution passive remote sensing and template matching. *Earth Surface Processes and Landforms*, *39*(7), 977–986. https://doi.org/10.1002/esp.3560

Hack, J. T. (1957). *Studies of longitudinal profiles in Virginia and Maryland* (Vol. 294, p. 95). US Government Printing Office. Retrieved from https://scholar.google.com/scholar_lookup?title=Studies of longitudinal profiles in Virginia and Maryland&author=J. Hack&publication_year=1957

Haviv, I., Enzel, Y., Whipple, K. X., Zilberman, E., Matmon, A., Stone, J., & Fifield, K. L. (2010). Evolution of vertical knickpoints (waterfalls) with resistant caprock: Insights from numerical modeling. *Journal of Geophysical Research: Earth Surface*, *115*(3), 1–22. https://doi.org/10.1029/2008JF001187

Hocini, N., Payrastre, O., Bourgin, F., Gaume, E., Davy, P., Lague, D., et al. (2021). Performance of automated methods for flash flood inundation mapping: A comparison of a digital terrain model (DTM) filling and two hydrodynamic methods. *Hydrology and Earth System Sciences*, *25*(6), 2979–2995. https://doi.org/10.5194/hess-25-2979-2021

Ijjasz-Vasquez, E. J., & Bras, R. L. (1995). Scaling regimes of local slope versus contributing area in digital elevation models. *Geomorphology*, *12*(4), 299–311. https://doi.org/10.1016/0169-555X(95)00012-T

Istanbulluoglu, E., & Bras, R. L. (2005). Vegetation-modulated landscape evolution: Effects of vegetation on landscape processes, drainage density, and topography. *Journal of Geophysical Research*, *110*(2), 1–19. https://doi.org/10.1029/2004JF000249

Johansen, K., Tiede, D., Blaschke, T., Arroyo, L. A., & Phinn, S. (2011). Automatic geographic object based mapping of streambed and riparian zone extent from LiDAR data in a temperate rural urban environment, Australia. *Remote Sensing*, *3*(6), 1139–1156. https://doi.org/10.3390/rs3061139

Kirby, E., & Whipple, K. X. (2012). Expression of active tectonics in erosional landscapes. *Journal of Structural Geology*, *44*, 54–75. https://doi.org/10.1016/j.jsg.2012.07.009

Lague, D. (2014). The stream power river incision model: Evidence, theory and beyond. *Earth Surface Processes and Landforms*, *39*(1), 38–61. https://doi.org/10.1002/esp.3462

Lague, D., & Davy, P. (2003). Constraints on the long-term colluvial erosion law by analyzing slope-area relationships at various tectonic uplift rates in the Siwaliks Hills (Nepal). *Journal of Geophysical Research*, *108*(B2). https://doi.org/10.1029/2002jb001893

Lague, D., & Feldmann, B. (2020). Topo-bathymetric airborne LiDAR for fluvial-geomorphology analysis. In J. F Shroder Jr. (Ed.), *Remote sensing of geomorphology* (pp. 25–54). Developmen. https://doi.org/10.1016/B978-0-444-64177-9.00002-3

Leopold, L., & Maddock, T. (1953). *The hydraulic geometry of stream channels and some physiographic implications*. *U.S. Geological Survey Professional, Paper 52*. US Government Printing Office.

LINZ. (2014). *Wellington 0.3m Rural Aerial Photos (2012–2013)*. Retrieved from https://data.linz.govt.nz/layer/51870-wellington-03m-rural-aerial-photos-2012-2013/

LINZ. (2017). *Wellington LiDAR 1m DEM (2013–2014)*. Retrieved from https://data.linz.govt.nz/layer/53621-wellington-lidar-1m-dem-2013-2014/

Lovill, S. M., Hahm, W. J., & Dietrich, W. E. (2018). Drainage from the critical zone: Lithologic controls on the persistence and spatial extent of wetted channels during the summer dry season. *Water Resources Research*, *54*(8), 5702–5726. https://doi.org/10.1029/2017WR021903

Manning, R. (1891). On the flow of water in open channels and pipes. *Transactions of the Institution of Civil Engineers of Ireland*, *20*(20), 161–207.

McNamara, J. P., Ziegler, A. D., Wood, S. H., & Vogler, J. B. (2006). Channel head locations with respect to geomorphologic thresholds derived from a digital elevation model: A case study in northern Thailand. *Forest Ecology and Management*, *224*(1–2), 147–156. https://doi.org/10.1016/j.foreco.2005.12.014

Montgomery, D. R., & Dietrich, W. E. (1992). Channel initiation and the problem of landscape scale. *Science*, *255*(5046), 826–830. https://doi.org/10.1126/science.255.5046.826

Montgomery, D. R., & Foufoula-Georgiou, E. (1993). Channel network source representation using digital elevation models. *Water Resources Research*, *29*(12), 3925–3934. https://doi.org/10.1029/93WR02463

Montgomery, D. R., & Gran, K. B. (2001). Downstream variations in the width of bedrock channels. *Water Resources Research*, *37*(6), 1841–1846. https://doi.org/10.1029/2000WR900393

Moore, I. D., & Burch, G. J. (1986). Sediment transport capacity of sheet and rill flow: Application of unit stream power theory. *Water Resources Research*, *22*(8), 1350–1360. https://doi.org/10.1029/wr022i008p01350

Moore, I. D., & Wilson, J. P. (1992). Length-slope factors for the revised universal soil loss equation: Simplified method of estimation. *Journal of Soil & Water Conservation*, *47*(5), 423–428.

Neal, J., Dunne, T., Sampson, C., Smith, A., & Bates, P. (2018). Optimisation of the two-dimensional hydraulic model LISFOOD-FP for CPU architecture. *Environmental Modelling & Software*, *107*, 148–157. https://doi.org/10.1016/j.envsoft.2018.05.011

O'Callaghan, J. F., & Mark, D. M. (1984). The extraction of drainage networks from digital elevation data. *Computer Vision, Graphics, and Image Processing*, *28*(3), 323–344. https://doi.org/10.1016/S0734-189X(84)80011-0

Orlandini, S., Tarolli, P., Moretti, G., & Dalla Fontana, G. (2011). On the prediction of channel heads in a complex alpine terrain using gridded elevation data. *Water Resources Research*, *47*(2), 1–12. https://doi.org/10.1029/2010WR009648

Passalacqua, P., Belmont, P., & Foufoula-Georgiou, E. (2012). Automatic geomorphic feature extraction from lidar in flat and engineered landscapes. *Water Resources Research*, *48*(3), 1–18. https://doi.org/10.1029/2011WR010958

Passalacqua, P., Belmont, P., Staley, D. M., Simley, J. D., Arrowsmith, J. R., Bode, C. A., et al. (2015). Analyzing high resolution topography for advancing the understanding of mass and energy transfer through landscapes: A review. *Earth-Science Reviews*, *148*, 174–193. https://doi.org/10.1016/j.earscirev.2015.05.012

Pavelsky, T. M., & Smith, L. C. (2008). RivWidth: A software tool for the calculation of river widths from remotely sensed imagery. *IEEE Geoscience and Remote Sensing Letters*, *5*(1), 70–73. https://doi.org/10.1109/LGRS.2007.908305

Perron, J. T., Dietrich, W. E., & Kirchner, J. W. (2008). Controls on the spacing of first-order valleys. *Journal of Geophysical Research*, *113*(4), 1–21. https://doi.org/10.1029/2007JF000977

Perron, J. T., & Royden, L. (2013). An integral approach to bedrock river profile analysis. *Earth Surface Processes and Landforms*, *38*(6), 570–576. https://doi.org/10.1002/esp.3302

PRISM. (2010). *PRISM Climate Group 30-year normals*. Oregon State University. Retrieved from https://prism.oregonstate.edu/normals/

Quinn, P., Beven, K., Chevallier, P., & Planchon, O. (1991). The prediction of hillslope flow paths for distributed hydrological modelling using digital terrain models. *Hydrological Processes*, *5*(1), 59–79. https://doi.org/10.1002/hyp.3360050106

Quinn, P. F., Beven, K. J., & Lamb, R. (1995). The in(α/tan/β) index: How to calculate it and how to use it within the topmodel framework. *Hydrological Processes*, *9*(2), 161–182. https://doi.org/10.1002/hyp.3360090204

Ramsey, L. A., Hovius, N., Lague, D., & Liu, C.-S. (2006). Topographic characteristics of the submarine Taiwan orogen. *Journal of Geophysical Research*, *111*(F2), F02009. https://doi.org/10.1029/2005JF000314

Roering, J. J., Mackey, B. H., Marshall, J. A., Sweeney, K. E., Deligne, N. I., Booth, A. M., et al. (2013). "You are HERE": Connecting the dots with airborne lidar for geomorphic fieldwork. *Geomorphology*, *200*, 172–183. https://doi.org/10.1016/j.geomorph.2013.04.009

Rowland, J. C., Shelef, E., Pope, P. A., Muss, J., Gangodagamage, C., Brumby, S. P., & Wilson, C. J. (2016). A morphology independent methodology for quantifying planview river change and characteristics from remotely sensed imagery. *Remote Sensing of Environment*, *184*, 212–228. https://doi.org/10.1016/j.rse.2016.07.005

Royden, L. H., Clark, M. K., & Whipple, K. X. (2000). Evolution of river elevation profiles by bedrock incision: Analytical solutions for transient river profiles related to changing uplift and precipitation rates. In *Eos, Transactions American Geophysical Union, Fall Meeting Supplement*.

Scheingross, J. S., Winchell, E. W., Lamb, M. P., & Dietrich, W. E. (2013). Influence of bed patchiness, slope, grain hiding, and form drag on gravel mobilization in very steep streams. *Journal of Geophysical Research: Earth Surface*, *118*(2), 982–1001. https://doi.org/10.1002/jgrf.20067

Schwenk, J., Khandelwal, A., Fratkin, M., Kumar, V., & Foufoula-Georgiou, E. (2017). High spatiotemporal resolution of river planform dynamics from Landsat: The RivMAP toolbox and results from the Ucayali River. *Earth and Space Science*, *4*(2), 46–75. https://doi.org/10.1002/2016EA000196

Schwenk, J., Piliouras, A., & Rowland, J. C. (2020). Determining flow directions in river channel networks using planform morphology and topology. *Earth Surface Dynamics*, *8*(1), 87–102. https://doi.org/10.5194/esurf-8-87-2020

Seidl, M. A., & Dietrich, W. E. (1992). The problem of channel erosion into bedrock. *Functional Geomorphology*, *23*, 101–124.

Snyder, N. P., Whipple, K. X., Tucker, G. E., & Merritts, D. J. (2000). Stream profiles in the Mendocino triple junction region, northern California. *GSA Bulletin*, *112*(8), 1250–1263. https://doi.org/10.1130/0016-7606(2000)112<1250:lrttfd>2.3.co;2

Snyder, N. P., Whipple, K. X., Tucker, G. E., & Merritts, D. J. (2003). Channel response to tectonic forcing: Field analysis of stream morphology and hydrology in the Mendocino triple junction region, northern California. *Geomorphology*, *53*(1–2), 97–127. https://doi.org/10.1016/S0169-555X(02)00349-5

Sofia, G., Tarolli, P., Cazorzi, F., & Dalla Fontana, G. (2015). Downstream hydraulic geometry relationships: Gathering reference reach-scale width values from LiDAR. *Geomorphology*, *250*, 236–248. https://doi.org/10.1016/j.geomorph.2015.09.002

Stock, J., & Dietrich, W. E. (2003). Valley incision by debris flows: Evidence of a topographic signature. *Water Resources Research*, *39*(4). https://doi.org/10.1029/2001WR001057

Stock, J. D., & Dietrich, W. E. (2006). Erosion of steepland valleys by debris flows. *Bulletin of the Geological Society of America*, *118*(9–10), 1125–1148. https://doi.org/10.1130/B25902.1

Tarboton, D. G. (1997). A new method for determination of flow directions and upslope in grid elevation models. *Water Resources Research*, *33*(2), 309–319. https://doi.org/10.1029/96wr03137

Tarboton, D. G. (2014). *Terrain analysis using Digital Elevation Models (TauDEM)*. Retrieved from http://hydrology.usu.edu/taudem/

Tarolli, P. (2014). High-resolution topography for understanding Earth surface processes: Opportunities and challenges. *Geomorphology*, *216*, 295–312. https://doi.org/10.1016/j.geomorph.2014.03.008

Tarolli, P., & Dalla Fontana, G. (2009). Hillslope-to-valley transition morphology: New opportunities from high resolution DTMs. *Geomorphology*, *113*(1–2), 47–56. https://doi.org/10.1016/j.geomorph.2009.02.006

Vergari, F., Troiani, F., Faulkner, H., Del Monte, M., Della Seta, M., Ciccacci, S., & Fredi, P. (2019). The use of the slope–area function to analyse process domains in complex badland landscapes. *Earth Surface Processes and Landforms*, *44*(1), 273–286. https://doi.org/10.1002/esp.4496

Whipple, K. X. (2004). Bedrock rivers and the geomorphology of active orogens. *Annual Review of Earth and Planetary Sciences*, *32*(1), 151–185. https://doi.org/10.1146/annurev.earth.32.101802.120356

Whipple, K. X., DiBiase, R. A., & Crosby, B. T. (2013). Bedrock rivers. *Treatise on Geomorphology*, *9*, 550–573. https://doi.org/10.1016/B978-0-12-374739-6.00254-2

Whittaker, A. C., Cowie, P. A., Attal, M., Tucker, G. E., & Roberts, G. P. (2007). Bedrock channel adjustment to tectonic forcing: Implications for predicting river incision rates. *Geology*, *35*(2), 103–106. https://doi.org/10.1130/G23106A.1

Willgoose, G., Bras, R. L., & Rodriguez-Iturbe, I. (1991). A coupled channel network growth and hillslope evolution model: 1. Theory. *Water Resources Research*, *27*(7), 1671–1684. https://doi.org/10.1029/91WR00935

Wobus, C., Whipple, K. X., Kirby, E., Snyder, N., Johnson, J., Spyropolou, K., et al. (2006). Tectonics from topography: Procedures, promise, and pitfalls. *Special Paper of the Geological Society of America*, *398*, 55–74. https://doi.org/10.1130/2006.2398(04)

Yanites, B. J. (2018). The dynamics of channel slope, width, and sediment in actively eroding bedrock river systems. *Journal of Geophysical Research: Earth Surface*, *123*(7), 1504–1527. https://doi.org/10.1029/2017JF004405

Yanites, B. J., Tucker, G. E., Mueller, K. J., Chen, Y. G., Wilcox, T., Huang, S. Y., & Shi, K. W. (2010). Incision and channel morphology across active structures along the Peikang River, central Taiwan: Implications for the importance of channel width. *Bulletin of the Geological Society of America*, *122*(7–8), 1192–1208. https://doi.org/10.1130/B30035.1

Zheng, X., Godbout, L., Zheng, J., McCormick, C., & Passalacqua, P. (2019). An automatic and objective approach to hydro-flatten high resolution topographic data. *Environmental Modelling & Software*, *116*(16), 72–86. https://doi.org/10.1016/j.envsoft.2019.02.007